논문개요집

ISSN 2233-9485(Print)
ISSN 2233-9574(Online)

2026년 한국자기학회 하계학술대회

2026 KMS Summer Conference

프로그램북

일시 2026. 6. 28(일) ~ 7. 2(목)
장소 한화리조트 해운대
주최 한국자기학회

Digests of the 2026 KMS Summer Conference
The Korean Magnetics Society

초대의 글

존경하는 한국자기학회 회원 여러분, 안녕하십니까.

올해 우리 학회는 전 세계 자성학 분야의 석학들과 연구자들이 모이는 국제 심포지엄인 ISAMMA 2026을 대한민국 부산에서 함께 개최하게 되었습니다.

세계적인 학술 대회의 성공적인 준비를 위해 힘써주신 조직위원회와 회원 여러분의 노고에 깊은 감사를 드립니다.

이번 2026년도 한국자기학회 하계 학술대회 및 임시총회는 ISAMMA 2026이라는 거대한 학술의 장과 더불어, 우리 학회 회원들이 한자리에서 긴밀하게 소통하고 학술적 성과를 나누는 뜻깊은 기회가 될 것입니다. 언제나 학회의 성장을 이끌어주시는 회원 여러분의 신뢰와 성원에 깊이 감사드립니다.

이번 학술대회는 급변하는 글로벌 기술 패권 경쟁 속에서 자성 및 스핀트로닉스 분야의 미래 대응 방안을 함께 고민하는 자리가 될 것입니다. 첨단 기술과의 유기적인 융합을 통해 우리 학회가 새로운 패러다임을 선도하고 한 단계 더 도약할 수 있는 중요한 전환점이 되기를 기대합니다. 이러한 집약된 논의를 통해 한국자기학회의 학문적 위상과 연구 역량이 더욱 넓은 세상으로 뻗어나가기를 확신합니다.

시원한 파도와 탁 트인 전망이 함께하는 해운대에서 다양한 분야의 최신 연구 동향을 경험하시고, 동료 연구자들과 함께 유익하고 창의적인 시간을 보내시기를 기원합니다. 회원 여러분의 많은 관심과 적극적인 참여를 부탁드립니다.

감사합니다.

2026. 6. 28

사단법인 한국자기학회 제18대 회장 **임 혜 인**

2026년 한국자기학회 하계학술대회 일정표

7월 2일[목] 오후

시간	프로그램		
08:30 ~	참가자 등록		
의과학자기 심포지엄 (3F 포럼1)		고효율 전력변환용 Ni-Free 자성페이스트 소재 및 부품화 기술개발 심포지엄 ㈜창성 (3F 포럼2)	
좌장: 김대홍(강원대)		좌장: 김성배((주)창성)	
14:00~14:20	곽민승 (동서대)	14:00~14:50	김성배 ((주)창성)
14:20~14:40	정경환 (강원대)		
14:40~15:00	백철하 (강원대)		
15:00~15:20	박신규 (강원대)	15:00~15:50	나재호 (넥스트 그리드)
15:20~15:30	COFFEE BREAK		
15:30~15:50	서정민 (부산가톨릭대)		
15:50~16:10	전필현 (대원대)	16:00~16:50	김기현 / 조주희 (한솔테크닉스 / KETI)
16:10~16:30	김경남 (가천대)		
16:30~17:00	POSTER DISCUSSION		
	좌장: 김대홍(강원대)		

CONTENTS

7월 2일(목) 14:00~17:00

심포지엄 의과학자기 (포럼1)

좌장 : 김대홍(강원대)

7월 2일(목) 14:00~17:00

Poster Session

Session MS [Magnetics in Medical Science] 좌장 : 김대홍(강원대)

7월 2일(목) 14:00~17:00

심포지엄 고효율 전력변환용 Ni-Free 자성페이스트 소재 및 부품화 기술개발 (포럼2)

좌장 : 김성배((주)창성)

2026 KMS Summer Conference

심포지엄 의과학자기

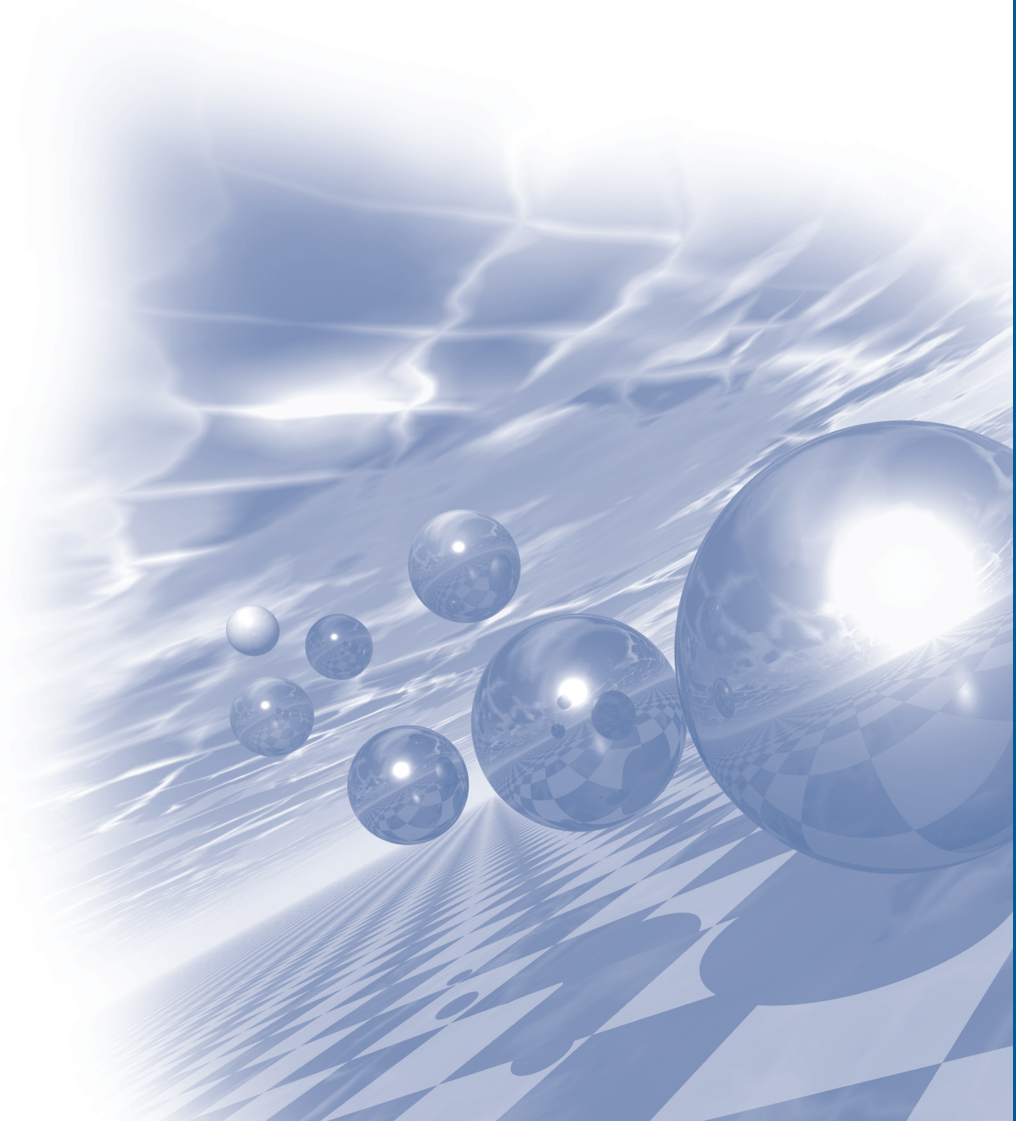

초S−1−1

Comparative Analysis of Single- and Multi-Level Wavelet U-Net Architectures for Low-Dose CT Restoration

Minseung Kwak[1*], MinJi Kwon[1], Byungdu Jo[1,2,3†]
[1]Department of Multidisciplinary Radiolgical Sciences, Dongseo University, Busan 47011, Korea
[2]Department of Radiological Sciences, Dongseo University, Busan 47011, Korea
[3]Center for Radiological Enviroment & Health Science, Dongseo University, Busan 47011, Korea

Computed tomography (CT) plays an essential role in clinical diagnosis; however, radiation exposure remains a major concern. Although low-dose CT (LDCT) can reduce patient radiation exposure, image noise and quality degradation may compromise diagnostic accuracy. Deep learning–based image restoration methods such as U-Net have demonstrated effective denoising performance, but limitations remain in preserving frequency-domain structural information. To address this issue, hybrid approaches integrating wavelet transform and deep learning have been proposed.

This study investigated the effect of wavelet decomposition depth on LDCT image restoration by comparing single-level and multi-level Wavelet→U-Net architectures under identical experimental conditions. Chest and abdomen CT images obtained from Kaggle were used in DICOM format. Gaussian noise with standard deviations ranging from 0.01 to 0.10 was added to simulate low-dose conditions. Each experiment was repeated five times under identical settings, and averaged results were used for evaluation. Quantitative analysis was performed using PSNR and SSIM metrics.

The proposed multi-level Wavelet→U-Net model achieved the highest performance with a PSNR of 36.55 dB and an SSIM of 0.94, outperforming both the single-level Wavelet→U-Net model and the conventional wavelet-based approach. Visual analysis also demonstrated improved noise suppression and enhanced structural preservation in thoracic regions. These results indicate that hierarchical wavelet decomposition can effectively improve LDCT image restoration performance while maintaining structural fidelity.

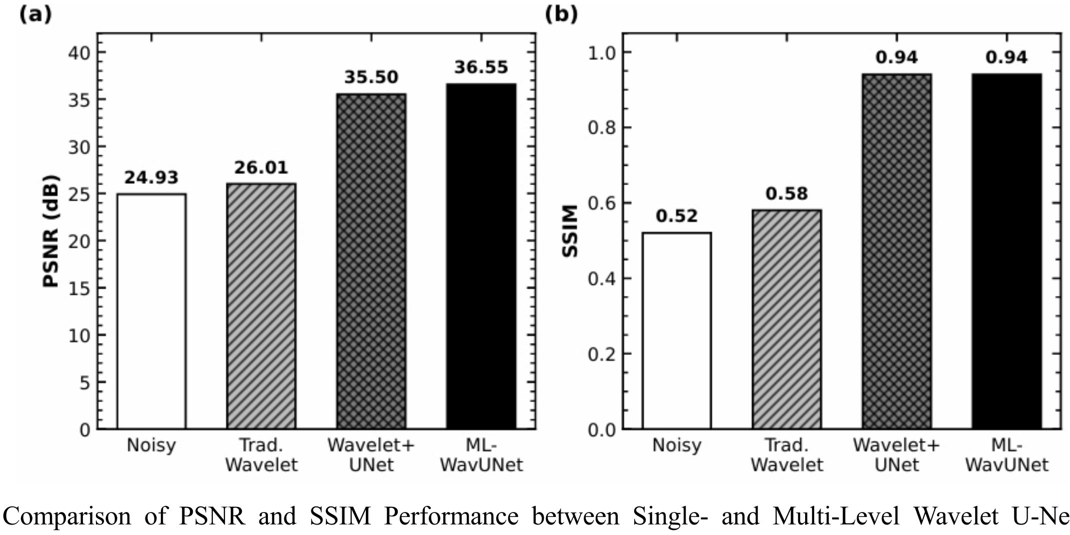

Fig. 1. Comparison of PSNR and SSIM Performance between Single- and Multi-Level Wavelet U-Net Models

초S－1－2

Validation of a Monte Carlo-Based 3D Printed CTDI Phantom for CT Dose Assessment

Jiseok Ko[1], Ki-Yoon Lee[1], Hyun-Dong Kim[1], Hyun-Soo Ha[1],
Kyung-Hwan Jung[1*†], Cheol-Ha Baek[2]

[1]Department of Health Medical Science, Kangwon National University, Samcheok, Korea
[2]Department of Radiological Science, Kangwon National University, Samcheok, Korea

Computed tomography(CT) is widely used in various clinical applications due to its ability to provide high-resolution visualization of internal anatomical structures. However, CT examinations involve relatively high radiation exposure, making accurate dose assessment and optimization essential. Currently, CT dose evaluation is primarily performed using commercially available CTDI(Computed Tomography Dose Index) phantoms; however, conventional phantoms are associated with high manufacturing costs and limited geometrical flexibility, restricting their applicability in educational and research settings. Accordingly, recent studies have focused on the development of 3D printing-based phantoms owing to their low production cost, rapid fabrication, and capability for customized geometric implementation. In this study, a 3D printed CTDI phantom was fabricated and its physical and imaging characteristics were compared with those of a commercial CTDI phantom(2-part PMMA CT Phantom, IBA Dosimetry) to evaluate its feasibility for CT dose assessment applications. For this purpose, a CT system and a CTDI head phantom(Ø160 × 150 mm) compliant with the IEC 60601-2-44 standard were modeled using the Monte Carlo simulation code MCNP(Monte Carlo N-Particle). The X-ray spectrum for the 130 kVp condition was generated using the SRS-78 program, and absorbed dose values were calculated using the F6 tally function in MCNP. Based on these results, CTDIw values were derived and compared with measured values obtained from the commercial phantom to validate the reliability of the simulation model. Subsequently, the CTDI phantom was designed using SolidWorks software and fabricated using a PLA+ filament-based 3D printing technique. The fabricated phantom was scanned using a Siemens SOMATOM go.Now 16-channel CT scanner under 130 kVp and 200 mAs conditions. CTDI_w values were calculated from CTDI_{100} measurements acquired at the central and peripheral positions of the phantom. In addition, HU values and image uniformity were evaluated. The results demonstrated that the CTDI_w values of the 3D printed phantom showed an average error within ±7.23% compared with those of the commercial phantom, while the mean HU difference was approximately +20 HU. Furthermore, image uniformity exhibited trends comparable to those of the commercial phantom. These findings indicate that the PLA+ based 3D printed CTDI phantom can provide dose evaluation performance comparable to that of a commercial CTDI phantom. Therefore, the proposed phantom may serve as a cost-effective and rapidly manufacturable alternative platform for educational, research, and customized CT dose assessment applications.

초S-1-3

Comparative Study of $LaBr_3$(Ce) and NaI(Tl) Detectors for PGNAA-Based Composition Analysis

Ki Yoon Lee[1,2], Kyungwan Jung[1], Hyun-Dong Kim[1], Hyun-Soo Ha[1],
Jung Hyeon Eo[2], Jun Young Shin[2], Jong Yul Kim[3], Jae Hyeon Kim[4], Kyung Min Oh[4],
Jin Hyung Park[4†], Cheol-Ha Baek[1,5*†]

[1]Department of Health Medical Science, Kangwon National University, Samcheok, Gangwon-do, Republic of Korea
[2]3I Solution Inc., Suwon, Gyeonggi-do, Republic of Korea
[3]Neutron Science Center, Korea Atomic Energy Research Institute, Daejun, Republic of Korea
[4]Advanced Radiation Technology Institute, Korea Atomic Energy Research Institute,
Jeongeup, Jeonbuk-do, Republic of Korea
[5]Department of Radiological Science, Kangwon National University, Samcheok, Gangwon-do, Republic of Korea

This study investigated the applicability of a $LaBr_3$(Ce) scintillation detector to thermal-neutron-based prompt gamma-ray neutron activation analysis (PGNAA) and compared its performance with that of a conventional NaI(Tl) detector for elemental identification and mass-fraction estimation. PGNAA spectra were measured at the Four-Circle Diffractometer (FCD) beamline of the HANARO research reactor at the Korea Atomic Energy Research Institute. The sample set consisted of pure Mn, Fe, Co, and Ni samples; binary Fe–Mn, Fe–Co, and Fe–Ni mixtures; and ternary NCM622 and NCM811 samples representing spent lithium-ion battery cathode materials. Elemental identification was conducted using Gaussian-derivative-convolution-based peak search, SNIP baseline correction, and Currie-criterion-based statistical validation. Mass fractions were estimated using region-of-interest-based weighted non-negative least squares (WNNLS) with attenuation-integration correction. The $LaBr_3$(Ce) detector provided higher Z-scores, smaller energy-matching errors, and more consistent characteristic peak combinations in mixed samples than the NaI(Tl) detector. For NCM622 and NCM811, $LaBr_3$(Ce) yielded mean absolute errors of 4.3 and 1.9 percentage points, respectively, and also showed higher R^2 values for spectral-shape reproduction. These results demonstrate that $LaBr_3$(Ce) can improve peak separation and compositional estimation in PGNAA-based nondestructive analysis of complex industrial materials, including spent lithium-ion battery cathodes.

Acknowledgements

This research was supported by the Technology Development Program of the Ministry of SMEs and Startups [RS-2024-00469068].

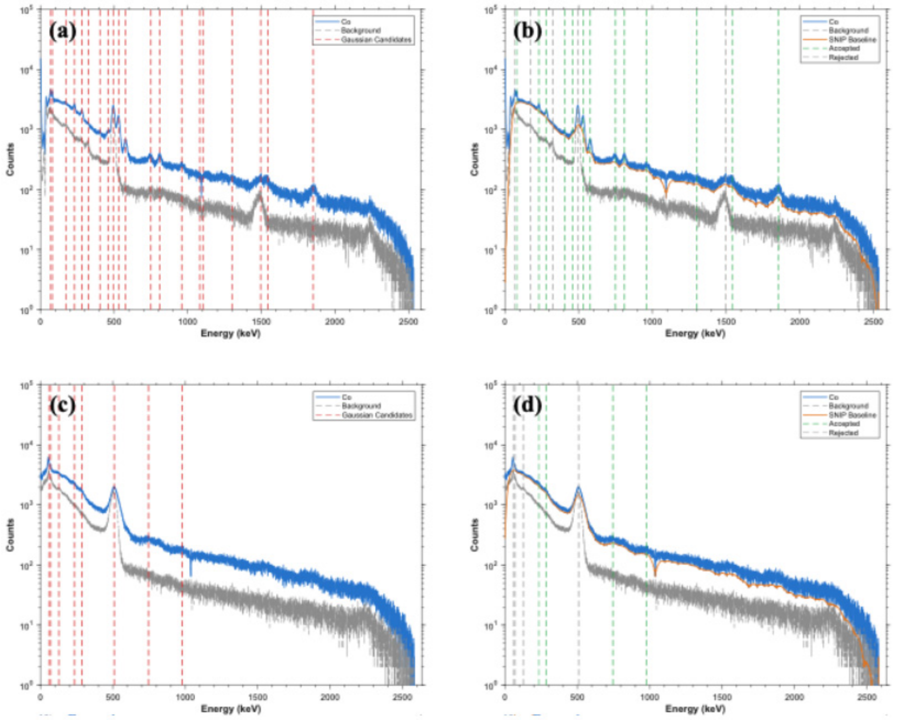

Fig. 1. Candidate peak detection and statistical validation results for the Co sample.
(a) Candidate peaks for $LaBr_3$(Ce), (b) accepted and rejected peaks after SNIP–Currie validation for $LaBr_3$(Ce), (c) candidate peaks for NaI(Tl), and (d) accepted and rejected peaks after validation for NaI(Tl).

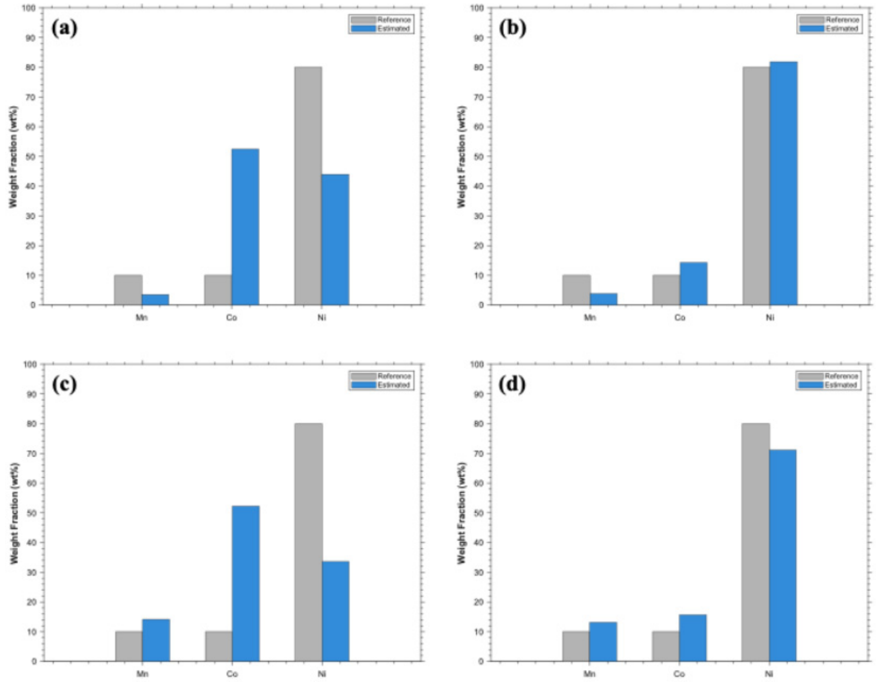

Fig. 2. Mass-fraction estimation results for the NCM811 sample.
(a) $LaBr_3$(Ce) with WNNLS, (b) $LaBr_3$(Ce) with WNNLS and attenuation-integration correction, (c) NaI(Tl) with WNNLS, and (d) NaI(Tl) with WNNLS and attenuation-integration correction.

초S-1-4

Measurement of Cerebral Cortex Activation Using Electroencephalography and Its Research Applications

Shin-Kyu Park[1*], Hoon-Jae Jeong[1], Bo-Kyoung Song[2†]
[1]Dept. of Occupational Therapy Graduate School, Kangwon National University, Korea
[2]Dept. of Occupational Therapy, Kangwon National University, Korea

Electroencephalography (EEG) is a non-invasive neurophysiological technique that records electrical activity generated by the cerebral cortex using electrodes placed on the scalp. Owing to its high temporal resolution, relatively low cost, and feasibility for repeated measurements, EEG has been widely utilized in clinical neuroscience and neurorehabilitation research. EEG signals reflect the summation of synchronized postsynaptic potentials generated by large populations of cortical neurons and are typically classified into delta wave (0.5–4 Hz), theta wave (4–8 Hz), alpha wave (8–13 Hz), beta wave (13–30 Hz), and gamma wave (>30 Hz) frequency bands. Electrode placement is commonly based on the international 10–20 system, and recorded signals undergo preprocessing procedures to remove artifacts such as eye blinks, muscle activity, and motion-related noise. Subsequently, frequency-domain and time–frequency analyses are applied to quantify cortical activation. Among the quantitative approaches for analyzing cortical activity, power spectral analysis and event-related desynchronization (ERD) are widely used. Power spectral analysis transforms EEG signals into the frequency domain to estimate the distribution of power across frequency bands, enabling objective evaluation of regional cortical activity and task-related changes. ERD refers to a task-related decrease in power relative to a baseline period and is predominantly observed in the alpha and beta bands over the sensorimotor cortex during motor execution and motor imagery. ERD reflects desynchronization of neuronal populations and is considered a direct indicator of cerebral cortex activation associated with motor processes. In stroke rehabilitation research, EEG-based assessment of cerebral cortex activation provides valuable insights into neural plasticity and motor recovery mechanisms. In particular, ERD patterns elicited during upper extremity movement or motor imagery tasks have been shown to reflect functional reorganization within the sensorimotor cortex and are associated with the level of upper extremity function. Furthermore, EEG-based neurorehabilitation approaches, including brain–computer interface (BCI), robot-assisted therapy, and neurofeedback, have demonstrated potential in promoting motor recovery by detecting and utilizing ERD in real time. The purpose of this presentation is to provide an overview of the fundamental principles of EEG, introduce power spectral and ERD analysis methods, and discuss their applications in the evaluation and rehabilitation of upper extremity function in individuals with stroke.

초S-1-5

Magnetic-Field-Based Charged-Particle Control for Dose Modulation and Active Radiation Protection

Jeong-Min Seo*†

Dept. of Radiological Science, Catholic University of Pusan, Korea

Charged particles(electrons, beta and alpha particles) can have their trajectories altered by magnetic fields.

Therefore, magnetic-field-based control of charged particles may provide an active radiation-protection strategy that differs from conventional passive shielding. This study presents an integrated series of investigations on the application of magnetic-field-based charged-particle control to diagnostic-radiation dose modulation and protection against charged particles, including beta particles, in radiation fields.

In an experimental study using a diagnostic X-ray generator, a static magnetic field of approximately 0.5 T was applied under tube-voltage conditions of 60–110 kVp, and dose measurements with and without the magnetic field were compared.

Small dose reductions were observed at 100 and 110 kVp, suggesting that the electron-associated dose component can be modulated by a magnetic field even under diagnostic-energy X-ray irradiation conditions.

The feasibility of a mobile charged-particle protection device for Cs-137 beta particles was evaluated using PHITS Monte Carlo simulations. A 1 Ci Cs-137 planar source was modeled, and an air dose-assessment volume was placed 30 cm from the source. Uniform dipole magnetic fields with effective lengths of 5 and 10 cm were applied. Under magnetic flux densities of 0.2–1.0 T, beta-particle absorbed dose reductions of more than approximately 88.7% were observed, indicating that a practical protection effect can be achieved even at approximately 0.2 T.

To further clarify the design conditions for compact and mobile shielding structures, the effective magnetic-field length was reduced to 1, 2, and 3 cm, and magnetic flux densities of 0.0–1.3 T were evaluated. In the 1 cm condition, the dose decreased with increasing magnetic flux density, but a dose rebound was observed in the high-field region. This was interpreted as trajectory over-deflection in a short magnetic-field region. In contrast, the 2 and 3 cm conditions showed practical saturation at approximately 0.4 and 0.3 T, respectively, with stable dose-reduction behavior. These findings indicate that the field–length product, rather than magnetic flux density alone, is a key design factor in magnetic-field-based charged-particle protection.

Overall, these studies demonstrate that magnetic-field-based charged-particle control can be extended from dose modulation in diagnostic radiology to compact and mobile active protection in radiation fields containing radioactive materials such as Cs-137. However, the Cs-137-related results should be interpreted as protection against the beta-particle/electron component, not as complete shielding of all Cs-137 radiation. Conventional passive shielding is still required for the 661.7 keV gamma-ray component.

Further studies incorporating realistic three-dimensional magnetic-field distributions, fringe fields, hybrid structures with passive gamma-ray shielding, quantitative evaluation of bremsstrahlung production, and experimental validation are required. With these developments, magnetic-field-based active protection may be applicable to localized protection of radiation workers, mobile survey instruments, robotic systems, and drone-based radiation monitoring platforms.

Verification of an Attenuation-Based Patient Size Method for Dose Estimation Using CT Cross-Sectional Images

Pil-Hyun Jeon*†, Da-Bin Do, Min-Ju Song

Department of Radiological Science, Daewon University, Korea

The growing use of CT has increased radiation exposure, emphasizing accurate dose estimation. Computed Tomography Dose Index (CTDIvol) does not account for patient size, while Size Specific Dose Estimate (SSDE) improves this but relies on labor-intensive manual AP and LAT measurements.

This study aims to verify an attenuation-based patient size estimation method using CT cross-sectional images and to evaluate its feasibility for accurate dose estimation. Water-equivalent diameter (Dw), considered the gold standard for patient size estimation, was calculated using pixel-based analysis of CT images. Specifically, pixel values above a threshold of -900 Hounsfield units were segmented, and attenuation-weighted area calculations were performed to derive Dw. Additionally, an attenuation-based patient size metric (ABPM) was proposed and compared with conventional geometric methods including AP, LAT, and AP+LAT.

The results demonstrated that AP+LAT showed the highest correlation with Dw ($R^2 = 0.9816$), while AP alone tended to overestimate SSDE. In contrast, attenuation-based methods (Dw and ABPM) more accurately reflected patient-specific attenuation characteristics and provided improved dose estimation. For example, using a CTDIvol of 6.0 mGy and a conversion factor based on Dw (f(Dw) = 1.35), SSDE was calculated as 8.12 mGy.

In conclusion, the attenuation-based pixel-derived Dw method provides a more realistic and reliable surrogate for patient size compared to conventional geometric approaches. This method enables more accurate SSDE calculation and has strong potential for automated, large-scale clinical implementation.

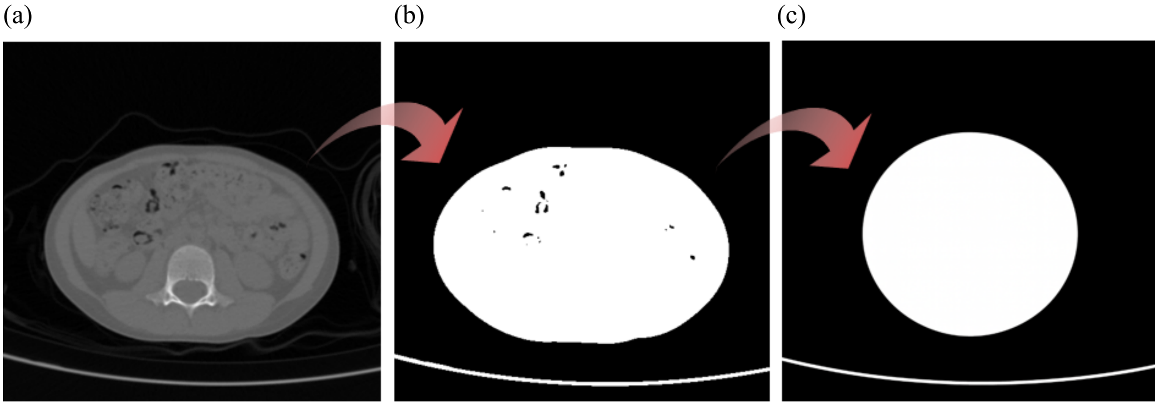

Fig. 1. Representative steps for measuring water-equivalent diameter (Dw) from an abdominal CT image: (a) original axial CT image, (b) pixel-based segmentation image, and (c) circle of area equivalent to total area of white pixels

초S-1-7

Indirect ^{10}B Concentration Analysis Based on ^{1}H Images at 11.74 T MRI

Daniel Hernandez[1], Taewoo Nam[2], Euwoo Lee[1], Young Seung Jo[1],
Jun-Young Chung[3†], Kyoung-Nam Kim[4*†]

[1]Gachon Biomedical Convergence Institute, Gachon University Gil Medical Center, Incheon, Korea
[2]Neuroscience Research Institute, Gachon University, Incheon, Korea
[3]Department of Neuroscience, College of Medicine, Gachon University, Incheon 21565, Republic of Korea
[4]Department of Biomedical Engineering, Gachon University, Seongnam, Korea

Introduction

The use of high-strength magnetic fields in magnetic resonance imaging (MRI), such as 11.74 T, provides a unique opportunity to image and acquire signals from nuclei other than hydrogen (^{1}H), which is typically used in conventional MRI. In contrast acquiring images of Boron (^{10}B) directly with MRI is complicated, therefore in this work we propose the indirect estimation of boron concentration through Boronophenylalanine (BPA) mixed with water by acquiring MRI images of phantoms with different concentrations. The images are analyzed using curve-fitting algorithms to estimate the corresponding concentrations.

Methods

A phantom was prepared capable of fitting 17 small cylindrical containers that were filled with different concentrations of water and Boronophenylalanine (BPA), which is a boron delivery agent. Table 1 shows the percentage of BPA per phantom. Magnetic resonance images (MRI) were taken with a 11.74T MRI scanner. The images were taken using a gradient echo with a matrix size of 512x256, images were taken in axial plane with 5 slices of 3mm thickness, a total of 36 images were taken with the combination of the following parameters, Repetition time (TR): 300, 500, 750 and 1000ms. Flip angle (FA): 30, 60 and 90°. Echo time (TE): 4.8, 6 and 10ms. Fig. 1 shows a diagram of the image parameter selection and its applications.

The data was prepared and preprocessed by first applying an image segmentation for each of the phantom containers with BPA concentration. Image normalization was also applied due to the magnetic field produced by the RF coil spatial distribution, with higher values near the coil and lower values at the center of the phantom. The normalization consisted on optimizing the correlation between the FA values and the BPA concentration. Finally, a curve fitting model was done using the computed as shown in Fig. 2, two models were implemented, one using a linear fitting based on image contrast and another using a logarithmic fitting model following the T2* relaxation decay.

Table 1. content of BPA in the mixture of water and boron in each phantom container.

Phantom number	1	2	3	4	5	6	7	8	9	10	11	12	13	14	15	16
BPA [%]	0	10	20	50	60	65	70	75	80	85	90	100	200	400	500	Null

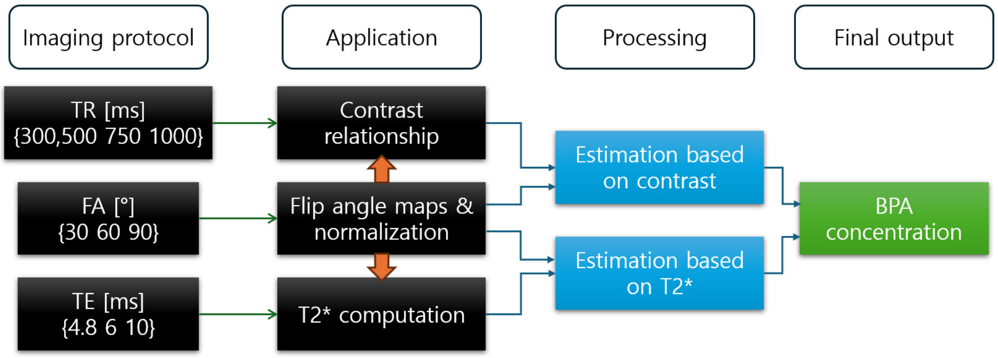

Fig. 1. The image parameters and applications for each image.

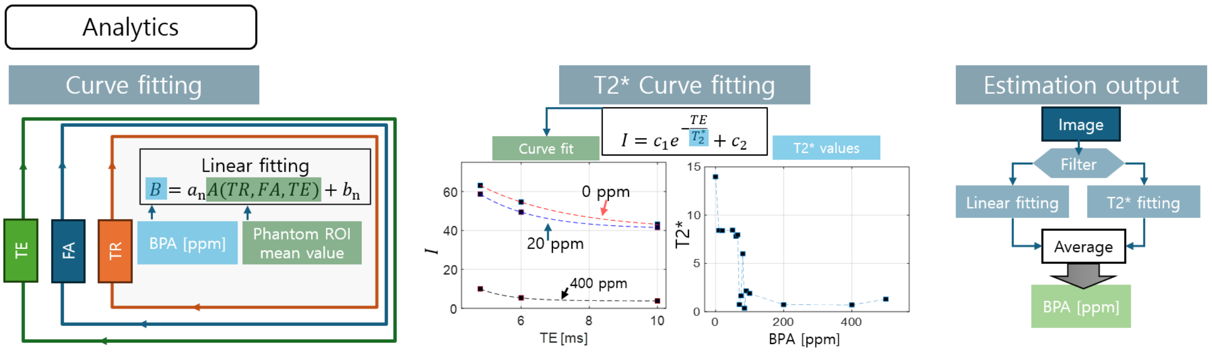

Fig. 2. The process of the applied analysis, for linear fitting, logarithm fitting for T2* and BPA final estimation.

Results

The images acquired with the phantoms are shown in Fig. 3, for different TRs. A total of 36 fits were done to determine which image parameters can provide the best linear fit. Fig. 4a and b shows the RMSE and R2 for each of the fits, the sRMSE with the lowest provides the best fit and the R2 close to 1 is considered the best fit as well, it was found that the image with FA of 30°, TR of 500ms, and TE of 4.8ms gave a RMSE of 0.001 and R2 of 0.999. By applying the curve fit to the normalized image, a map of the BPA concentration could be computed as shown in Fig 4c. The logarithm fit (Fig. 4d) and the computed T2* maps (Fig. 4e) are used to compute the second estimation of BPA (Fig. 4e) and finally the average value between Fig. 4c-e gives the final BPA estimation.

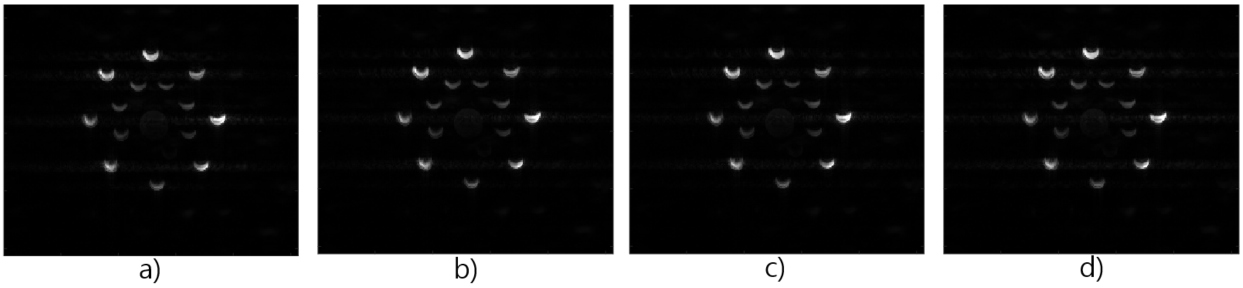
a) b) c) d)

Fig. 3. The images with TE4.8, FA 30° and TR of a) 300ms, b) 500ms, c) 750ms, d) 1000ms.

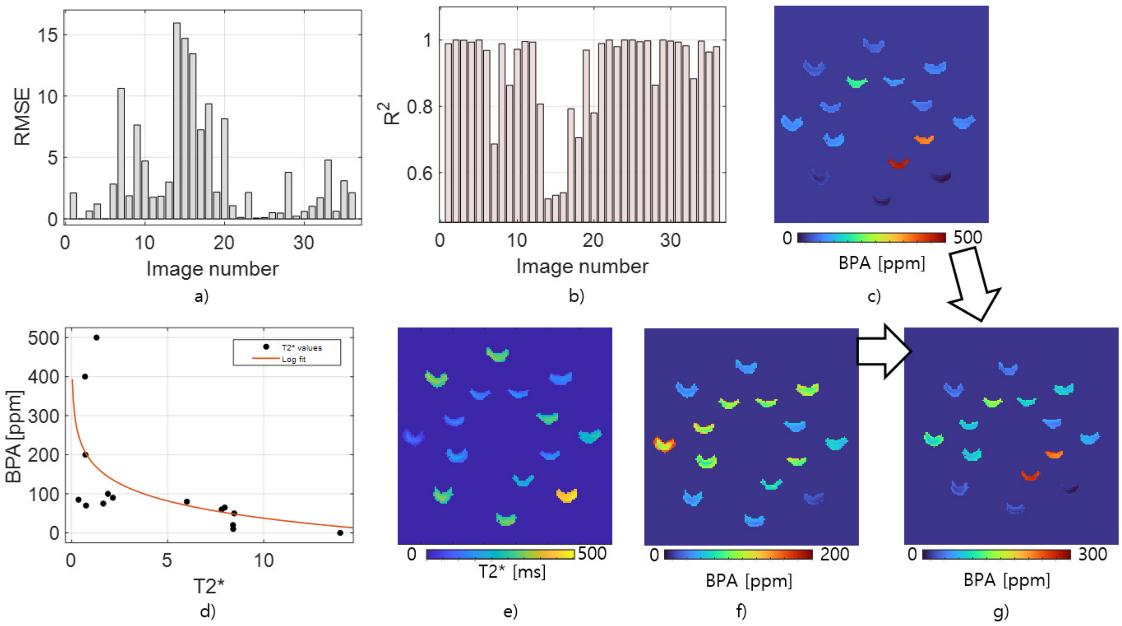

Fig. 4. The results from the analysis, for the linear curve fitting a) RMSE, b) R2, c) the computed BPA maps from linear fitting, d) the logarithm curve fitting, e) T2* maps, f) computed BPA maps from T2* and g) the combination by averaging c and f.

Conclusions

This study presents the implementation of algorithms for estimating BPA concentration based on water mixtures. The estimation had an 80% accuracy. The current approach has some limitations, such as the need for image normalization and the use of strong image filters. These issues can be addressed by acquiring higher-quality MRI images, minimizing motion artifacts through improved phantom design, and enhancing RF coil performance to achieve more uniform |B1|-field distributions.

Acknowledgement

This work was supported by the National Research Foundation of Korea(NRF) grant funded by the Korea government(MSIT) (RS-2025-02303425) and supported by a grant of the Korea Health Technology R&D Project through the Korea Health Industry Development Institute (KHIDI), funded by the Ministry of Health & Welfare, Republic of Korea (grant number : RS-2025-24536397) and supported by the Gachon University Gil Medical Center (Grant number: FRD2025-15).

포스터발표

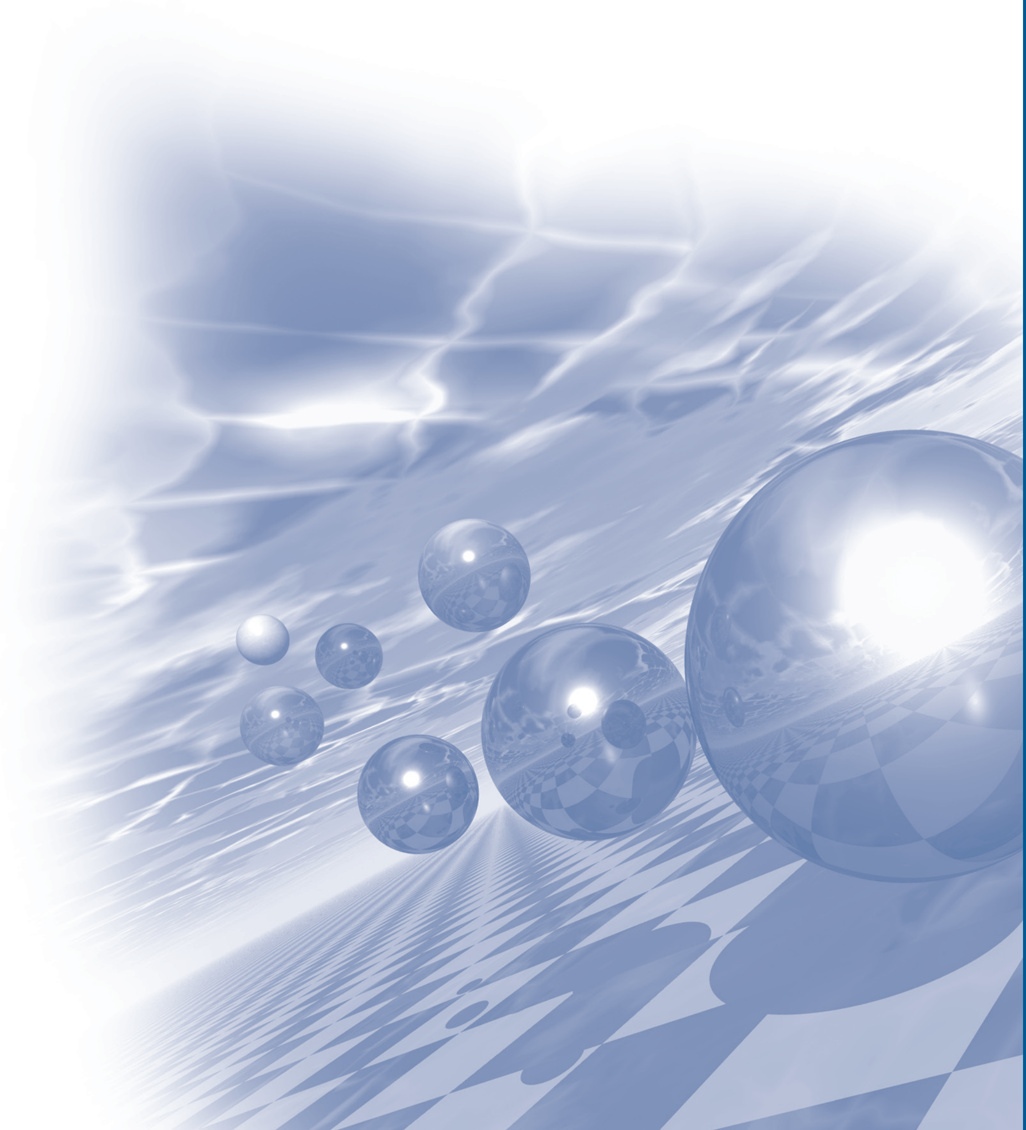

Design of a DOI Detector through Analysis of Signal Magnitude According to the Interaction Position Between the Scintillator and Electromagnetic Radiation

Seung-Jae Lee[1,2*]

[1]Department of Radiological Science, Dongseo University, Korea
[2]Center for Radiological Environment & Health Science, Dongseo University, Korea

Small-animal Positron Emission Tomography (PET) often suffers from degraded spatial resolution at the periphery of the field of view. To mitigate this issue, it is essential to determine the precise location of gamma-ray interactions within the scintillator, known as the depth of interaction (DOI). In this study, we designed a DOI-capable detector utilizing a single-layer scintillator block (3 x 3 x 20 mm) coupled with a Multi-Pixel Photon Counter (MPPC) consisting of a 4 x 4 pixel array.To evaluate the detector's performance, the DETECT2000 simulation tool was used to model the behavior of optical photons within the crystal. Gamma-ray interaction events were simulated at intervals ranging from 2.5 mm to 5 mm along the scintillator. The resulting energy spectrum, derived from the MPPC signals, exhibited four distinct peaks corresponding to each interaction site. Analysis showed that events occurring closer to the MPPC appeared in higher channels, while those further away appeared in lower channels. These results suggest that the proposed detector design can effectively determine the interaction depth of gamma rays, thereby improving PET image resolution.

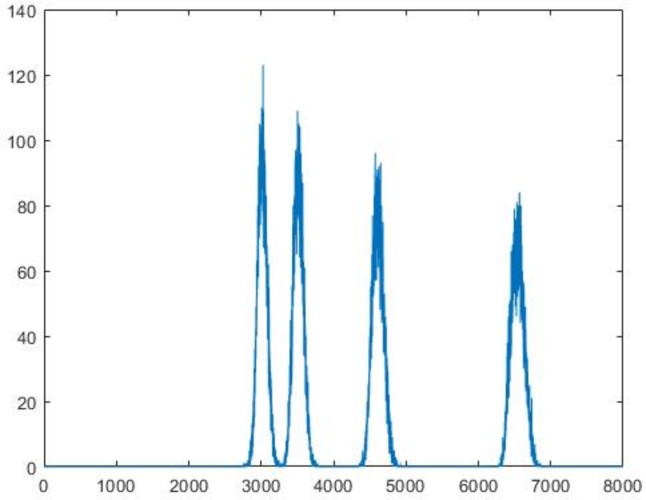

Fig. 1. Distribution in the energy spectrum according to the magnitude of the signal acquired by interaction with electromagnetic radiation at each scintillator height.

MS02

Development of a DOI Detector Using Scintillation Pixel Arrays with Different Sizes for Each Layer

Seung-Jae Lee[1,2*]

[1]Department of Radiological Science, Dongseo University, Korea
[2]Center for Radiological Environment & Health Science, Dongseo University, Korea

A two-layer depth of interaction (DOI) detector was developed to improve the spatial resolution of PET/MRI with a small gantry. The scintillation pixel arrays in each layer are sized 6 ◈ 6 and 9 ◈ 9, and they are arranged in a misaligned manner. This misalignment enables the light generated in each layer to be collected by the light sensor in a different distribution, such that the images of the scintillation pixels in each layer are imaged at different locations in the flood image. To evaluate the DOI performance of the detector, a flood image was acquired using a Na-22 electromagnetic radiation source that emits positrons. As a result, all the scintillation pixels in the two layers were separated and measured. It was confirmed that the distance at which the scintillation pixels were imaged was larger than the spatial resolution of each scintillation pixel image. A PET/MRI system with a small gantry configured using this detector is expected to achieve excellent spatial resolution.

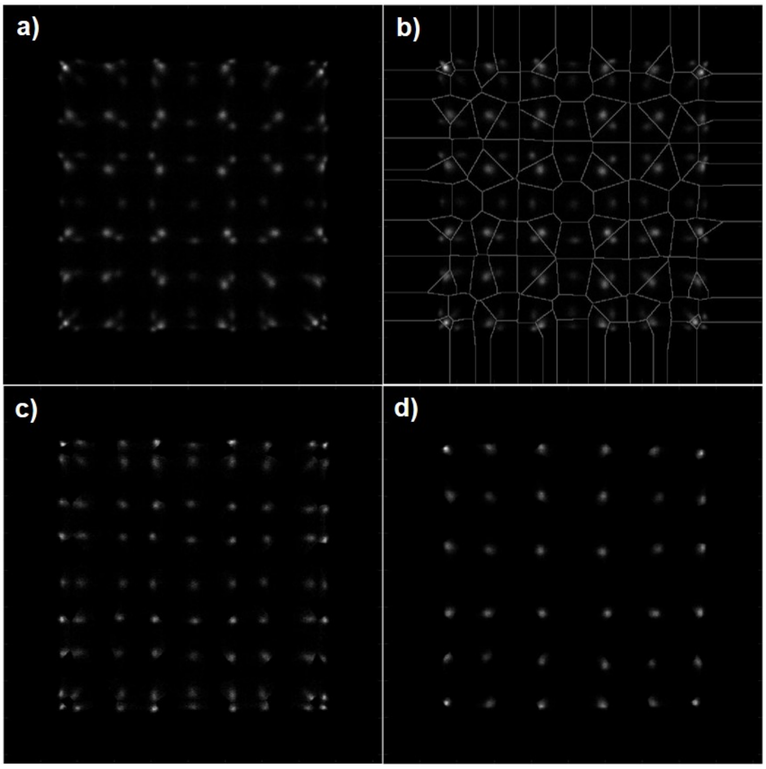

Fig. 1. Flood image acquired via a DOI detector. a) Flood image of two-layer scintillation block, b) segmentation of the flood image in a), flood image of the scintillation pixel array that forms the c) bottom layer and d) top layer.

MS03

Development of a Method for Fast Electromagnetic Radiation Measurement as a Solution to Signal Pile-Up by Measuring the Rising Slope of the Signal Waveform

Seung-Jae Lee[1,2*], Cheol-Ha Baek[3†]

[1]Department of Radiological Science, Dongseo University, Korea
[2]Center for Radiological Environment & Health Science, Dongseo University, Korea
[3]Department of Radiological Science, Kangwon National University, Korea

Detection systems based on photon counting utilize a system that makes use of a dedicated application specific integrated circuit (ASIC) for very fast electromagnetic radiation measurement. However, even with a high-speed system, the signal pile-up phenomenon still occurs. In this study, a general-purpose method that can measure radiation very fast, and can measure electromagnetic radiation lost due to pile-up was developed. This method determines the energy by analyzing the signal waveform, and by converting the rising slope of the signal into energy. Analysis of the slope, instead of measuring the entire waveform, enables the measurement time to be greatly reduced, and by measuring the rising slope, each individual electromagnetic radiation signal can be separated and measured even in signals where pile-up occurred. This method, which eliminates the need for a dedicated ASIC, can be applied to existing systems. In addition, this method is expected to enable a very efficient detection system to be developed because the loss of photon counting can be minimized in high electromagnetic radiation fields.

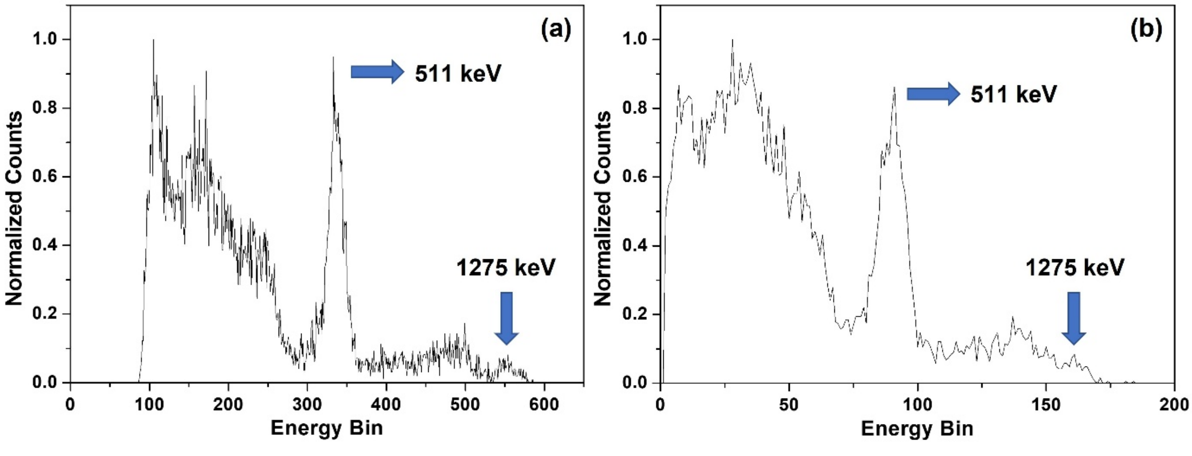

Fig. 1. Energy spectrum of the Na-22 electromagnetic radiation source displayed using the data acquisition. (a) Energy spectrum constructed by measuring all the waveforms of the signal, (b) Energy spectrum constructed by measuring the slope.

MS04

Physics-Constrained and Attention-Guided Deformable Image Registration for Adaptive Radiotherapy

Byungdu Jo[1,2,3*†]

[1]Department of Multidisciplinary Radiological Sciences, The Graduate School of Dongseo University, Busan 47011, Korea
[2]Department of Radiological Sciences, Dongseo University, Busan 47011, Korea
[3]Center for Radiological Environment & Health Science, Dongseo University, Busan 47011, Korea

Adaptive radiotherapy (ART) requires accurate deformable image registration to align planning computed tomography and daily treatment images. However, daily cone-beam CT or treatment-room images often suffer from scatter, low contrast, anatomical deformation, and non-linear intensity differences. These limitations may reduce the reliability of organ-at-risk localization, target matching, and dose accumulation. Therefore, a registration framework that preserves anatomical boundaries while suppressing non-physical deformation is essential for clinically robust ART workflows.

In this study, we propose PDADR-Net, a physics-constrained dual-attention deformable registration network. The network uses a shared 3D encoder for fixed and moving volumes and applies token-pooled cross-attention at two spatial scales to capture long-range correspondence with reduced computational burden. A progressive flow decoder estimates dense forward and inverse deformation fields, and a differentiable 3D spatial transformer generates the registered volume.

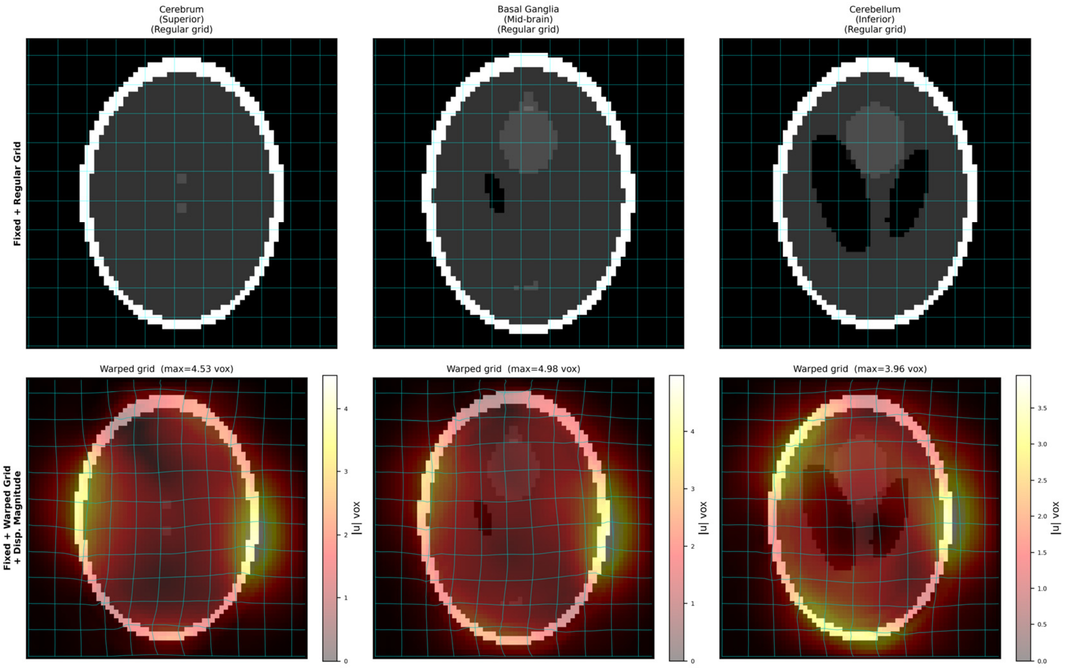

Fig. 1. Deformation grid visualization for the 3D Shepp–Logan brain phantom. Fixed reference images with regular grids are shown in the upper row, while the lower row displays warped grids overlaid with displacement magnitude maps at three anatomical slice levels.

The objective function combines five complementary constraints: structural topology-preserving similarity (STPS), normalized cross-correlation, gradient-weighted mutual information (GWMI), deformation smoothness, and inverse consistency. STPS jointly evaluates intensity similarity, gradient-magnitude similarity, and Jacobian determinant variance to encourage boundary alignment and topology preservation. GWMI further emphasizes high-gradient anatomical interfaces using a Parzen-window mutual information formulation. Phantom validation was performed using a 64^3 3D Shepp-Logan phantom and an organ-realistic thorax phantom with smooth random deformations. Registration quality was assessed using SSIM, NCC, deformation magnitude, Jacobian statistics, and negative-Jacobian percentage.

The preliminary implementation demonstrates a boundary-aware and topology-constrained framework for 3D deformable registration. PDADR-Net may provide a technical basis for fast and reliable image alignment in ART, particularly for future pCT-CBCT registration, synthetic CT-based dose recalculation, and motion-aware dose accumulation studies.

MS05

Effects of 5 Hz HF-rTMS Combined with VFSS-Based Oral Action Observation Training on Mu-Band ERSP and Bolus Transit Time in PSD

JaeHoon Jeong[1*], Shin-Kyu Park[2], Bo-Kyoung Song[3†]

[1]Dept. of Occupational Therapy Graduate School, Kangwon National University, Korea
[2]Dept. of Occupational Therapy, Kangwon National University, Korea
[3]Dept. of Occupational Therapy, Kangwon National University, Korea

This study aimed to investigate the effects of 5 Hz high-frequency repetitive transcranial magnetic stimulation (HF-rTMS) combined with videofluoroscopic swallowing study (VFSS)-based action observation (AO) training on swallowing-related cortical activation and bolus transit in patients with post-stroke dysphagia (PSD). Six patients participated in this study and were divided into an experimental group (n=3) and a control group (n=3). The experimental group received 5 Hz HF-rTMS combined with AO training, whereas the control group received sham rTMS combined with AO training. The intervention was conducted three times per week for four weeks, with each session lasting 30 minutes. In the experimental group, 5 Hz HF-rTMS was applied to the suprahyoid muscle-related motor cortical area for 10 minutes, followed by 20 minutes of oral and swallowing-related AO training. Cortical activation was measured using electroencephalography (EEG) during the AO task. For EEG analysis, the -1 to 0 s period before AO onset was set as the baseline, and the subsequent 10 s AO period was analyzed. The C3, Cz, and C4 electrodes were defined as the region of interest (ROI), and event-related spectral perturbation (ERSP) in the mu rhythm band was analyzed. Swallowing function was assessed using VFSS with a C-arm X-ray system (DK Medical Solution, Republic of Korea). VFSS images were recorded at 30 frames per second, and each frame was converted to approximately 0.033 s. Oral transit time (OTT) and pharyngeal transit time (PTT) were calculated frame by frame. After the intervention, the experimental group showed decreased mu-band power in the C3, Cz, and C4 areas, suggesting increased sensorimotor cortical activation during oral and swallowing-related AO. In addition, decreases in OTT and PTT were observed, indicating improved temporal efficiency of bolus transit during the oral and pharyngeal phases. In the control group, changes in cortical activation and bolus transit time were less evident. These findings suggest that 5 Hz HF-rTMS combined with VFSS-based AO training may facilitate swallowing-related cortical activation and improve oropharyngeal bolus transit in patients with PSD.

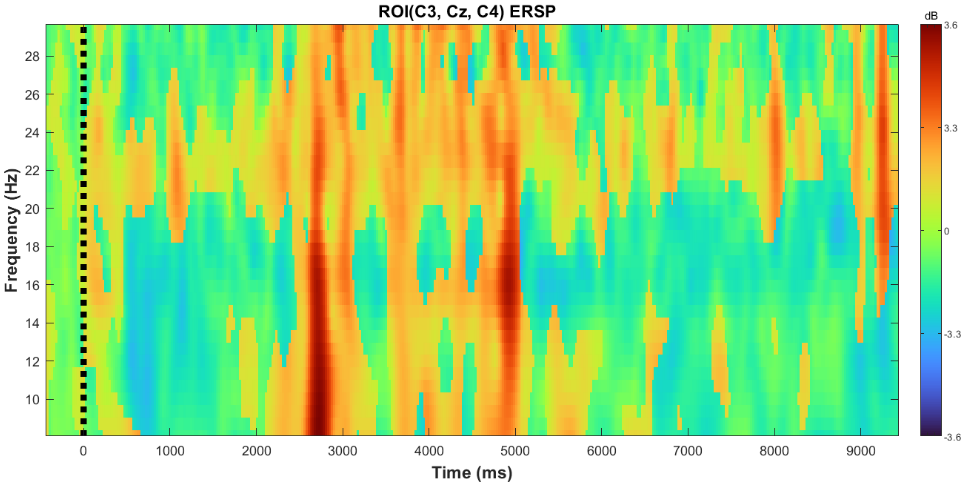

Pre-intervention

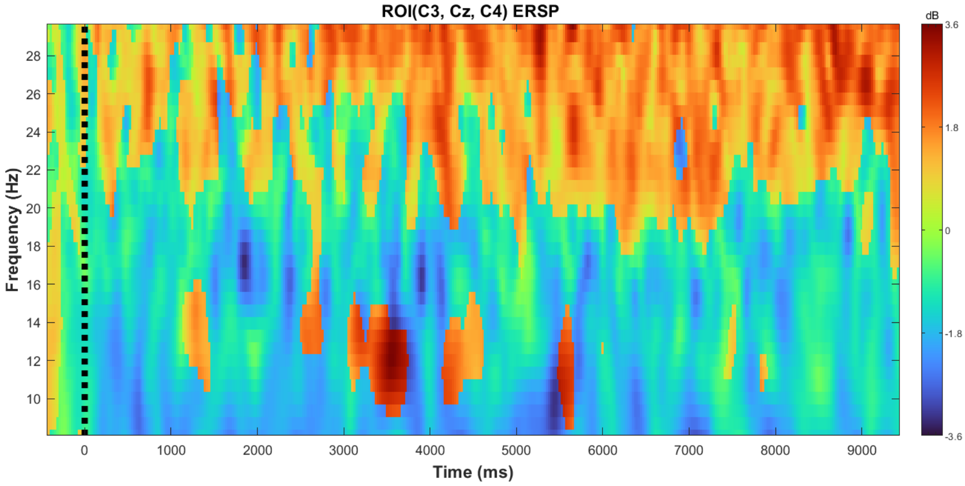

region of interest : ROI, event-related spectral perturbation

Post-intervention

Fig. 1. Before and after intervention changes in mu-band ERSP during AO in the ROI (C3, Cz, C4).

Table 1. Before and after intervention changes in OTT and PTT between two groups

Variable	Group	Before	After	Change
OTT (sec)	5 HF-rTMS/AO group	3.42 ± 0.38	3.16 ± 0.35	-0.26
OTT (sec)	sham rTMS+ AO group	3.35 ± 0.36	3.28 ± 0.34	-0.07
PTT (sec)	5 HF-rTMS/AO group	1.58 ± 0.17	1.19 ± 0.15	-0.39
PTT (sec)	sham rTMS+ AO group	1.24 ± 0.16	1.22 ± 0.15	-0.02

high frequency: HF, repetitive transcranial magnetic stimulation: rTMS, action observation: AO, oral transit time: OTT, pharyngeal transit time: PTT.

MS06

Preliminary Evaluation of EEG-to-ECG Signal Transformation Using a 1D U-Net

Seungmin Hwang[1*], Sun-woo Lee[1], Jiyoung Ahn[2], Young-Jin Jung[3†]
[1]Department of Biomedical Engineering, Chonnam National University, Korea
[2]School of Biomedical Engineering, Chonnam National University, Korea
[3]School of Healthcare Biomedical Engineering, Chonnam National University, Korea

The feasibility of an EEG-to-ECG transformation model for estimating electrocardiography (ECG) waveforms from electroencephalography (EEG) signals was preliminarily evaluated in this study. ECG is a biosignal that directly reflects the electrical activity of the heart and is widely used for heart-rate and beat-interval analysis. However, simultaneous ECG measurement during EEG recording requires the attachment of additional electrodes, which increases the complexity of the experimental setup and may increase user burden during long-term monitoring or wearable applications. Meanwhile, EEG recordings may contain not only neural activity but also physiological components originating from cardiac activity. Therefore, these components may be utilized to estimate heart-related information without additional ECG electrodes.

Accordingly, a 1D U-Net-based regression model was constructed using segment-wise multichannel EEG signals as input. The 1D U-Net can reflect both local temporal features and overall waveform structures, and it was designed to reconstruct ECG-like waveforms from input EEG signals through an encoder-decoder architecture. Prior to model inference, channel-wise mean removal was applied to reduce baseline differences within each segment, and array-shape correction was performed to match the model input format. The ECG waveforms predicted by the model were compared with the reference ECG under both raw-amplitude and z-score-normalized conditions.

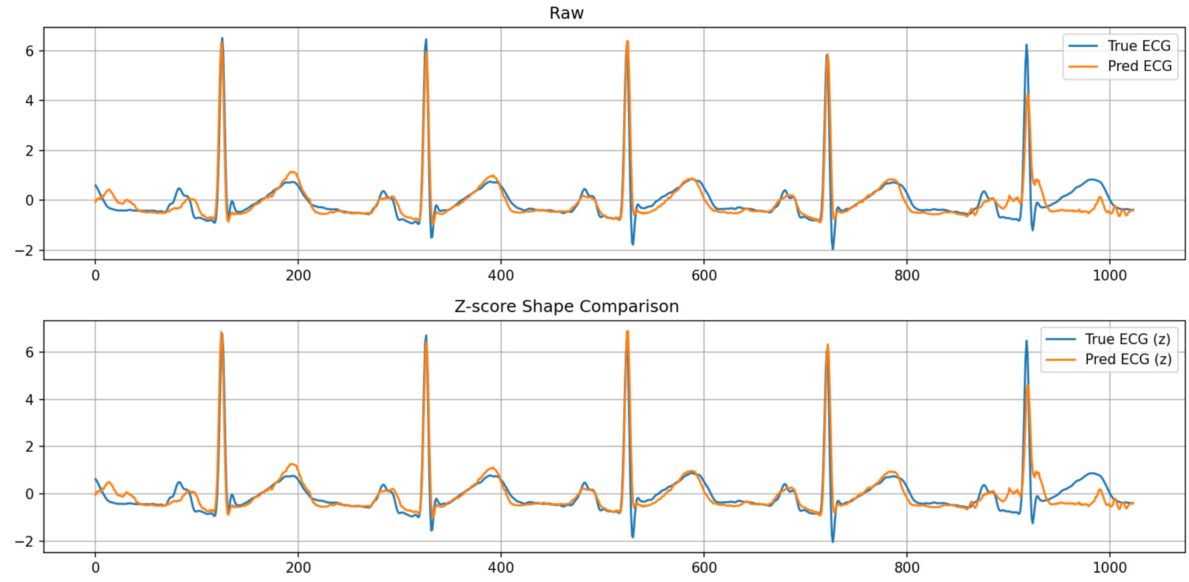

Fig. 1. True vs predicted ECG waveforms

Analysis of representative segments showed that the predicted ECG generally reproduced the major R-peak timing and repetitive beat intervals of the reference ECG. In addition, some P- and T-wave morphologies and overall waveform variations showed similar tendencies. In particular, under z-score normalization, the major temporal patterns of the two signals remained similar even after reducing the influence of amplitude differences. However, underestimation of R-peak amplitude, local waveform distortion, and baseline differences were observed in some sections. These results suggest that a deep learning model based on multichannel EEG can partially reconstruct the major temporal characteristics of ECG, particularly R-peak timing and cardiac rhythm information. In future work, the generalization performance of the model will be evaluated using quantitative metrics, including the Pearson correlation coefficient, RMSE, MAE, R-peak detection accuracy, and heart-rate error, with validation across various subjects and measurement conditions.

A Web-Based Platform for Streamlined EEG Signal Analysis and Visualization

Jiyoung Ahn[1*], Seungmin Hwang[2], Sun-woo Lee[2], Young-Jin Jung[3†]
[1]School of Biomedical Engineering, Chonnam National University, Korea
[2]Department of Biomedical Engineering, Chonnam National University, Korea
[3]School of Healthcare Biomedical Engineering, Chonnam National University, Korea

Electroencephalography (EEG) is a widely used non-invasive technique for studying brain dynamics in both research and clinical settings. However, existing analysis tools such as EEGLAB and MATLAB-based pipelines often require complex software installation, licensing costs, and programming expertise, limiting accessibility for researchers without engineering backgrounds. Furthermore, the lack of integrated visualization and pipeline management in conventional tools results in fragmented workflows that hinder reproducibility and collaboration. To lower these barriers, we developed a web-based EEG analysis platform that requires no installation and runs entirely in a browser. The proposed platform was developed as a web-based application. It provides a multi-channel signal viewer (up to 32 ch) with real-time pre-filtering, power spectral density (PSD) analysis via Welch's method, topographic scalp mapping, spectrogram visualization, and a node-based visual pipeline editor that allows users to construct, save, and reuse customized analysis workflows without programming. The platform was tested using a 32-channel synthetic EEG dataset. PSD analysis correctly identified spectral peaks at the assigned frequency for all 32 channels. Band power distribution across the five frequency bands was visualized per channel, consistent with the synthetic signal design. Topographic maps and spectrograms provided spatially and temporally coherent visualizations. The proposed platform demonstrates that a fully web-based, installation-free environment can deliver accurate and comprehensive EEG analysis. By removing technical and financial barriers associated with conventional EEG software, the platform has the potential to broaden access to quantitative EEG tools across diverse research and clinical environments. In particular, the node-based pipeline editor enables standardized and reusable analysis protocols, which is especially valuable in multi-site studies or longitudinal research where consistency across sessions is critical, while remaining accessible to researchers and clinicians without dedicated computational resources or programming expertise.

Development of an MR-Compatible Temporal Interference Stimulation Device

Sun-woo Lee[1*], Seungmin Hwang[1], Jiyoung Ahn[2], Young-Jin Jung[3†], Sukhoon Oh[4†]

[1]Department of Biomedical Engineering, Chonnam National University, Korea
[2]School of Biomedical Engineering, Chonnam National University, Korea
[3]School of Healthcare Biomedical Engineering, Chonnam National University, Korea
[4]Unit for Bio-imaging Translational Research, Korea Basic Science Institute, Cheongju, Korea

Temporal interference stimulation (TIS) is a non-invasive electrical stimulation technique which uses two high-frequency alternating currents to produce beat pulses. These currents have slightly different frequencies, creating a low-frequency interference pattern in a deep brain area. To interpret and evaluate TIS, the stimulation device needs to be operated under magnetic resonance imaging (MRI) conditions. In this study, we developed an MRI-compatible TIS device for use in phantom-based MRI experiments, and evaluated its operational feasibility in gradient-echo (GRE) imaging conditions.

The MR-TIS system was designed to generate two sinusoidal current outputs at frequencies of 2000 Hz and 2001 Hz, thereby creating a TIS condition with an offset frequency of 1 Hz. The output current and stimulation duration were set to 5 mA and 5 ms, respectively. An MRI evaluation was performed using a 120 × 120 × 120 mm^3 electrically conductive phantom, with 10 mm-wide copper electrodes attached to its surface at a 50 mm. The system consisted of a control unit, a waveform generation unit, an output current control unit, an electrode interface, and an MRI-compatible connection structure. Phase images of GRE were acquired while the dual-frequency stimulation was applied to the phantom.

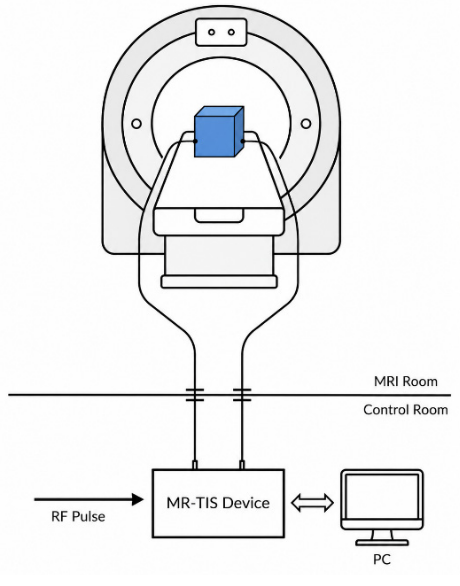

Fig. 1. Experimental setup and block diagram of the MR-compatible TIS system in the MRI environment.

The TIS device successfully generated stimulation outputs of 2000 Hz and 2001 Hz under MRI operating conditions, maintaining a target amplitude of 5 mA throughout the 5 msec stimulation period. During GRE phase scans, the stimulation process was performed without any apparent operational interference between the MR-TIS device and the MRI system. No stimulation-induced image artifacts or increases in image noise were observed in the GRE phase images. These results indicate that the developed MR-compatible TIS device can operate during MRI acquisition without significantly degrading of phase image quality.

The developed MR-compatible TIS device can be used as a hardware platform for MRI-based TIS experiments. The proposed system will facilitate further studies on electrode configuration, stimulation current conditions, cable-induced interference, and image-based evaluation methods for transcranial electrical stimulation (tES) applications.

MS09

Analysis of Additional Gamma-Ray Attenuation by MRI Magnetic Shielding Materials in a PET/MRI Environment

YoungMin Choi[1,2*], Suhyoung Lee[2], Jaeyoung Park[2], Sangrok Kim[2†], Manseok Han[1,3†]

[1]Department of Health Medical Science, Graduate School, Kangwon National University, Samcheok , Korea
[2]Radiation Safety Section, Korea Institute of Radiological and Medical Sciences, Seoul, Korea
[3]Department of Radiological Science, Kangwon National University, Samcheok , Korea

PET/MRI is a hybrid imaging modality that simultaneously provides metabolic and functional information from positron emission tomography (PET) and superior soft-tissue contrast and anatomical information from magnetic resonance imaging (MRI)[1]. However, the 511 keV annihilation gamma rays generated from PET can be emitted into the surrounding environment. Therefore, in PET/MRI rooms, not only electromagnetic shielding for MRI operation but also evaluation of radiation shielding characteristics is required[2]. Conventional MRI rooms are mainly designed with RF shielding and magnetic field shielding, and dedicated shielding for PET gamma rays may not be sufficiently considered[3]. Therefore, in this study, under the condition that copper was fixed as the RF shielding material of an MRI room, the additional shielding effect of MRI magnetic shielding materials against 511 keV gamma rays generated from PET was evaluated using PHITS simulation.

In this study, a 511 keV monoenergetic photon pencil beam was used. To simulate the RF shielding material of an MRI room, a copper (Cu) RF shielding layer with a thickness of 0.01 cm was placed. The distance between the source and the RF shielding layer was set to 1 m, and the MRI magnetic shielding material was placed immediately behind the RF shielding layer. A water phantom with a radius of 1 cm was placed behind the shielding material as the detection region to calculate the effective dose-converted value after shielding. Lead (Pb) was selected as the reference shielding material, and silicon steel, low-carbon steel, plate steel, Mu-metal, and NiZn ferrite were selected as candidate MRI magnetic shielding materials. The density and chemical composition of each material were reflected in the PHITS input. The thicknesses of the magnetic shielding materials were varied as 1, 2, 3, 5, and 10 cm. Effective dose evaluation was performed using the fluence-to-effective-dose conversion multiplier based on ICRP Publication 103 implemented in PHITS, and the results were calculated as effective dose-converted values in pSv/source[4]. By comparing the effective dose-converted values under each shielding condition, the shielding efficiency, first tenth-value layer (TVL_1), and equilibrium tenth-value layer (TVL_e) were calculated.

The effective dose-converted values decreased with increasing shielding thickness for all materials. Pb showed a rapid decrease from 0.231 pSv/source at 1 cm to 0.009 pSv/source at 3 cm, and exhibited very low effective dose-converted values at thicknesses greater than 5 cm. Among the MRI magnetic shielding materials, Mu-metal showed the lowest effective dose-converted values. The values for Mu-metal decreased from 0.586 pSv/source at 1 cm to 0.035 pSv/source at 5 cm and 0.001 pSv/source at 10 cm. Steel-based materials, including silicon steel, low-carbon steel, and plate steel, showed similar trends, with values of approximately 0.053–0.058 pSv/source at 5 cm and approximately 0.002–0.003 pSv/source at 10 cm. NiZn ferrite showed the highest effective dose-converted values among the compared materials, with 0.775 pSv/source at 1 cm, 0.152 pSv/source at 5 cm, and 0.019 pSv/source at 10 cm [Fig. 1]. In the TVL_1 and TVL_e analysis, Pb showed the lowest values of 1.37 cm and 1.35 cm, respectively, indicating the best attenuation performance. Among the MRI magnetic shielding materials, Mu-metal showed the lowest values, with TVL_1 of 3.25 cm and TVL_e of 3.20 cm. Steel-based materials showed similar attenuation characteristics, with TVL_1 values ranging from 3.68 to 3.79 cm and TVL_e values ranging from 3.64 to 3.73 cm. In contrast, NiZn ferrite showed the highest values, with TVL_1 of 5.59 cm and TVL_e of 5.54 cm, indicating that the greatest thickness was required to achieve the same attenuation level [Fig. 2]

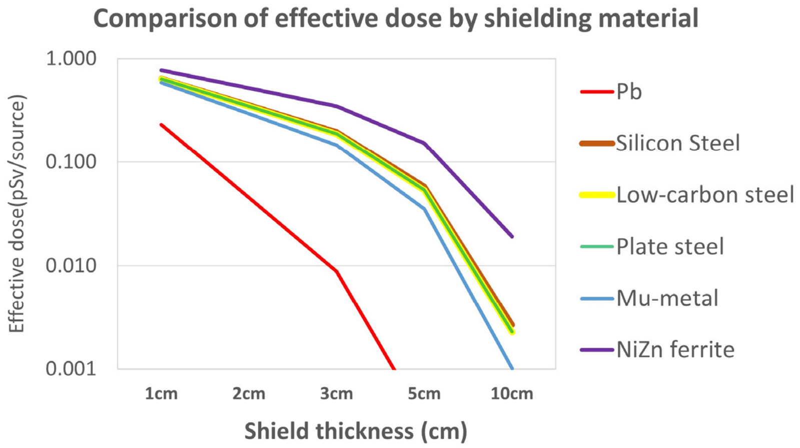

Fig. 1. Comarison of effective dose by shielding material

Shielding material	TVL_1	TVL_e
Pb	1.370	1.350
Silicon steel	3.790	3.730
Low-carbon steel	3.680	3.640
Plate steel	3.690	3.640
Mu-metal	3.250	3.200
NiZn ferrite	5.590	5.540

Fig. 2. Comparison of TVL_1 and TVL_e by shielding material

The results of this study demonstrated that MRI magnetic shielding materials provide a certain level of additional attenuation against PET 511 keV gamma rays. In particular, steel-based materials, which can be used as magnetic shielding materials in actual MRI rooms, showed a reduction in effective dose with increasing thickness, suggesting that existing MRI shielding structures may partially contribute to the reduction of PET gamma rays. However, Pb showed the highest shielding performance at the same thickness, indicating that MRI magnetic shielding materials alone have limitations in completely replacing dedicated radiation shielding materials. Although Mu-metal showed the best attenuation performance among the MRI magnetic shielding materials, its cost and constructability should be considered for application as a large-area shielding material in actual MRI rooms. Therefore, in the shielding design of PET/MRI rooms, the additional attenuation effect of MRI shielding materials can be considered; however, the need for dedicated shielding materials for radiation protection should also be evaluated. Further simulations reflecting the actual PET/MRI room structure and scatter build-up effects are required.

This study was supported by a grant of the Korea Institute of Radiological and Medical Sciences(KIRAMS), funded by Ministry of Science and ICT(MSIT), Republic of Korea. (No.50422-2026)

References

[1] Bailey DL, Antoch G, Bartenstein P, Barthel H, Beer AJ, Bisdas S, et al. Combined PET/MR: The real work has just started. Mol Imaging Biol.2015;17(3):297-312. doi:10.1007/s11307-015-0848-4.

[2] Madsen MT, Anderson JA, Halama JR, Kleck J, Simpkin DJ, Votaw JR, et al. AAPM Task Group 108: PET and PET/CT shielding requirements. Med Phys.2006;33(1):4-15. doi:10.1118/1.2135911.

[3] Elster AD. Radiofrequency shielding. MRIQuestions.com. Available from: https://mriquestions.com/why-rf-shielding.html

[4] Sato T, Iwamoto Y, Hashimoto S, Ogawa T, Furuta T, Abe S, et al. Features of Particle and Heavy Ion Transport code System PHITS version 3.02. J Nucl Sci Technol.2018;55(6):684-690. doi:10.1080/00223131 2017.1419890.

MS10

Evaluation of the Effect of ^{18}F-FDG Injected Activity on PET Imaging in the 9.4 T Ultra-High Magnetic Field Small-Animal MR Environment

Yeonghun Song[1,2*], Chan Oh[1], Cheol-Ha Baek[2†], Jangwoo Park[1†]
[1]Korea Radioisotope Center for Pharmaceuticals, Korea Institute of Radiological & Medical Sciences, Korea
[2]Department of Medical Health Science, Kangwon National University, Korea

PET/MR은 PET의 대사・기능 정보와 MR의 우수한 연부조직 대조도 및 해부학적 정보를 동시에 제공할 수 있어 임상 및 전임상 소동물 영상 연구에서 활용되고 있다. 그러나 기존 전임상용 PET/MR 연구는 주로 4.7 T 이하의 MR 환경에 집중되어 있으며, 9.4 T 이상의 초고자장 환경에서 PET insert를 이용한 소동물 PET/MR 연구는 아직 제한적이다. 초고자장 환경에서는 positron range 감소에 따른 PET signal blurring 감소와 spatial resolution 개선 가능성이 보고되어 있으나, 실제 전임상 조건에서 투여 방사능 농도에 따른 PET 정량성 평가는 충분히 비교되지 않았다. 이에 본 연구는 9.4 T 초고자장 소동물용 MR 환경에서 ^{18}F-FDG 투여농도가 주요 장기의 SUV 정량값에 미치는 영향을 평가하고, 저투여량 조건에서도 장기 단위 SUV 정량 분석이 가능한지 확인하고자 하였다.

실험은 mouse 9마리를 대상으로 진행되었고 ^{18}F-FDG PET/MR 영상을 획득하였다. 각 mouse의 체중은 약 19 ± 1 g으로 일정하였으며, 목표 투여 방사능에 따라 400, 200, 50 μCi의 3개 군으로 분류하였다. 각 군은 n=3으로 구성하였다. ^{18}F-FDG 주입 후 60분의 uptake time을 두었고, 이후 20분간 PET acquisition과 MR image acquisition을 동시에 수행하였다. 영상 획득에는 9.4 T 소동물용 MRI 시스템(BioSpec 94/20, Bruker)과 insert PET System(SimPET, Brightonix)을 사용하였다. ROI는 MR anatomical information을 기반으로 Brain, Liver, Kidney, Muscle에 설정하였다. PMOD VOI statistics에서 SUV averaged, standard deviation 값을 산출하였고, ROI 내부 SUV 분포의 상대적 변동성을 평가하기 위해 변동계수(CV)를 계산하였다. 통계 분석은 GraphPad Prism software를 이용하여 수행하였으며, 각 투여군 간 SUV averaged 및 CV의 차이는 one-way ANOVA로 분석하였다.

50, 200, 400 μCi 세 군에서 Brain, Liver, Kidney, Muscle의 SUV averaged와 ROI 내부 변동계수(CV)를 비교하였다 (Table 1). One-way ANOVA 결과, SUV averaged는 Brain, Liver, Kidney, Muscle 모두에서 투여군 간 유의한 차이를 보이지 않았다($p>0.05$). 또한 ROI 내부 SUV 분포의 상대적 변동성을 나타내는 CV 역시 모든 ROI에서 유의한 군 간 차이를 보이지 않았다($p>0.05$) (Table 2). 이는 50 μCi 저투여량 조건에서도 주요 장기의 SUV averaged와 ROI 내부 상대적 변동성이 200 및 400 μCi 조건과 비교하여 유의한 차이를 보이지 않았음을 의미한다. 따라서 본 연구 결과는 9.4 T 초고자장 소동물용 MR 환경에서 PET 영상 획득 시, 50 μCi 수준의 저투여량 조건에서도 주요 장기의 SUV 정량 분석이 가능함을 확인하였다. 다만 본 연구에서는 MRI sequence 차이에 따른 PET 영상 정량값 및 영상 품질의 영향을 평가하지 못하였으므로, 향후 RF pulse 및 gradient 조건이 다른 다양한 MRI sequence를 적용하여 PET 정량 안정성과 PET/MR 동시 획득 조건에서의 상호 영향을 추가적으로 검증할 필요가 있다.

Acknowledgements

이 연구는 과학기술정보통신부(MSIT)의 재원으로 한국원자력의학원(KIRAMS)의 지원을 받아 수행되었음 (No.50539-2026, RI융복합 첨단 선도기술 기반 신약개발 지원 및 운영)

Table 1. Organ SUV averaged and SD values by ^{18}F-FDG injected activity.

Dose	mouse no.	Brain	Liver	Kidney	Muscle
50uCi	Mouse 1	1.15±0.14	0.35±0.02	0.62±0.16	0.45±0.04
50 uCi	Mouse 2	1.19±0.15	0.31±0.05	0.54±0.11	0.60±0.08
50 uCi	Mouse 3	1.13±0.18	0.29±0.02	0.48±0.10	0.58±0.11
200 uCi	Mouse 4	1.23±0.17	0.36±0.03	0.58±0.11	0.51±0.04
200 uCi	Mouse 5	1.55±0.20	0.33±0.01	0.63±0.17	0.86±0.04
200 uCi	Mouse 6	1.30±0.14	0.36±0.01	0.53±0.09	0.87±0.12
400 uCi	Mouse 7	1.27±0.14	0.31±0.01	0.64±0.17	0.74±0.12
400 uCi	Mouse 8	1.48±0.23	0.41±0.05	0.67±0.16	1.16±0.19
400 uCi	Mouse 9	1.29±0.16	0.32±0.02	0.57±0.12	0.75±0.15

Table 2. One-way ANOVA results for (a) SUV averaged values and (b) ROI CV values.

(a)

ROI	F Statistic	P-value
Brain	2.681933	0.147189
Liver	0.936704	0.442553
Kidney	1.300167	0.339553
Muscle	2.528942	0.159749

(b)

ROI	F Statistic	P-value
Brain	0.29978	0.751465
Liver	0.749296	0.512289
Kidney	0.337878	0.726027
Muscle	3.880499	0.08289

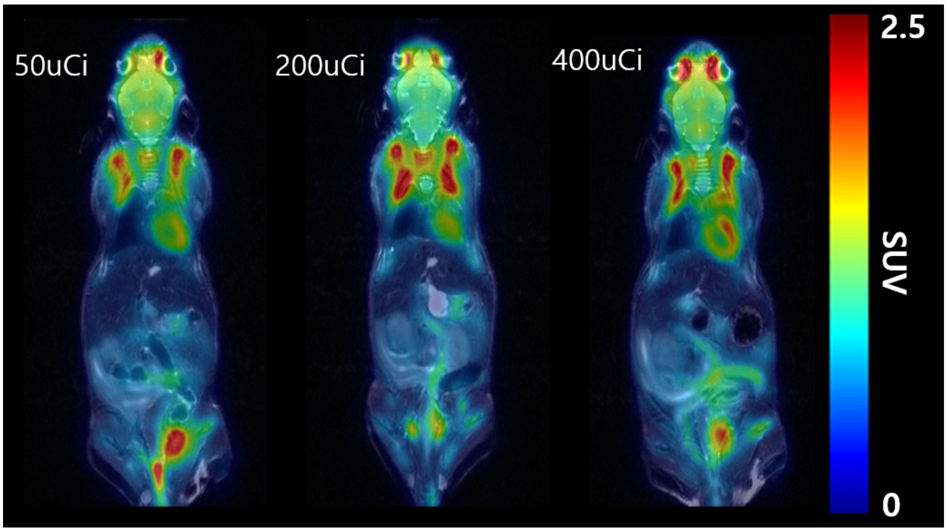

Fig. 1. Representative ^{18}F-FDG PET/MR Images

MS11

Light Distribution Analysis in a Quasi-monolithic DOI-PET Detector

Donggeun Roh[1*], Junho Kang[1], Seoui Kang[2], Yugang Kim, Yurim Song[2], Jihoon Kang[1,2,3,4†]
[1]Chonnam National University, Department of Biomedical Engineering, Graduate School, Yeosu, South Korea
[2]Chonnam National University, Department of Biomedical Engineering, Yeosu, South Korea
[3]Chonnam National University, School of Biomedical Engineering, Yeosu, South Korea
[4]Chonnam National University, Research Center for Healthcare-Biomedical Engineering, Yeosu, Korea

본 연구에서는 quasi-monolithic 섬광결정이 삽입된 3층 DOI-PET 검출기에 대해 W-ratio를 적용하여 DOI 층 간 광분포 분리 특성을 분석하였다. 검출기는 두 층으로 구성된 4×4 배열의 $3\times3\times10\ \text{mm}^3$ LSO 픽셀형 섬광결정층 사이에 $3\times12\times\text{T}\ \text{mm}^3$ quasi-monolithic LSO 층을 삽입한 구조로 구성하였으며, quasi-monolithic 층의 두께(T)는 1 mm에서 10 mm까지 1 mm 간격으로 변화하였다.

DETECT2000 기반 몬테카를로 시뮬레이션을 통해 광신호를 획득하였으며, 각 이벤트에 대해 최대 광신호와 전체 광신호 합의 비율인 W-ratio를 계산하였다. 이후 실제 감마선 반응 깊이에 따라 Bottom, Middle, Top 층으로 데이터를 분류하고, 각 층의 W-ratio 분포를 histogram 기반으로 분석하였다. 또한 층 간 분포 차이를 정량적으로 평가하기 위하여 정규화된 분포 분리 지표를 적용하였다. 분석 결과, quasi-monolithic 층 두께 증가에 따라 DOI 층 간 분포 분리 특성이 향상되는 경향이 관찰되었다. 해당 지표는 값이 증가할수록 DOI 층 간 분포 분리 특성이 우수함을 의미한다. Top-Middle 분리도는 1 mm에서 0.172, 10 mm에서 0.767로 증가하였으며, Middle-Bottom 분리도는 0.143에서 0.838로 증가하였다. 또한 Top-Bottom 분리도는 0.027에서 2.421까지 증가하여 가장 높은 층 분리 특성을 나타냈다. 이러한 결과는 quasi-monolithic 층 두께 증가에 따라 광확산 특성이 변화하며 DOI 층 간 광분포 차이가 보다 명확하게 형성됨을 의미한다. 본 연구에서 제안한 W-ratio 기반 분석 방법은 quasi-monolithic DOI-PET 검출기의 결과는 W-ratio 기반 분석을 통해 quasi-monolithic 층의 광확산 특성과 DOI 층 간 분포 변화를 평가할 수 있음을 보여준다. 향후 DOI 분류 알고리즘의 입력 특징 및 검출기 최적화 지표로 활용 가능할 것으로 기대된다.

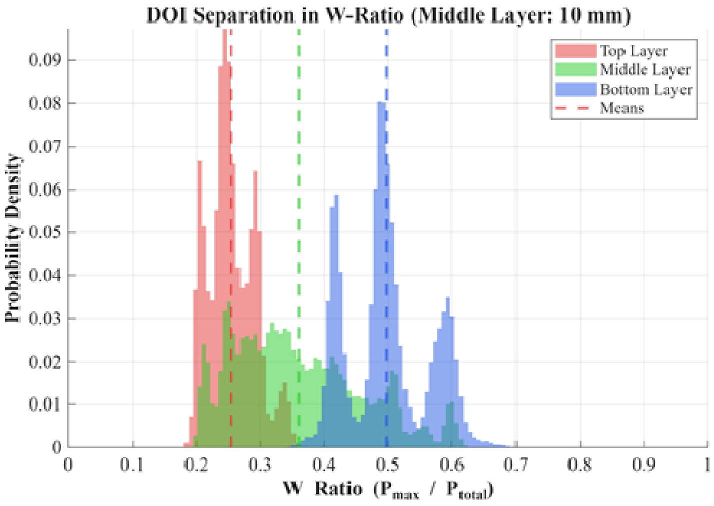

Fig. 1. W-ratio distributions for each DOI layer in the DOI-PET detector with a 10 mm quasi-monolithic layer

MS12

Impact of Image Preprocessing on Deep Learning-Based Bone Metastasis Classification in Whole-Body Bone Scintigraphy Using Patient-Level Cross-Validation

Jeong-Ho Kim*, Chae-Yoon Jeong†
Department of Radiological Science, Konyang University, Korea

Purpose: This study aimed to evaluate the impact of image preprocessing methods on deep learning-based bone metastasis classification performance in whole-body bone scintigraphy (WBBS) using patient-level cross-validation designed to minimize data leakage.

Materials and Methods: The publicly available BS-80K dataset was used in this study. To reduce potential data leakage, patient identifiers were extracted from image filenames, and patient-level 10-fold cross-validation was performed so that images from the same patient were assigned to only one fold. Folders containing fewer than 20 abnormal images were excluded. Four preprocessing conditions were evaluated: Original image, Histogram Equalization (HE), Contrast Limited Adaptive Histogram Equalization (CLAHE), and Gaussian Blur. Preprocessing was applied on-the-fly within the dataset pipeline. A ResNet-18 model pretrained on ImageNet was used for binary classification of normal and abnormal WBBS images. Training conditions were fixed across all preprocessing methods. Performance was evaluated using area under the receiver operating characteristic curve (AUC), accuracy, sensitivity, and specificity. Pairwise AUC comparisons were performed using paired t-tests with Holm–Bonferroni correction.

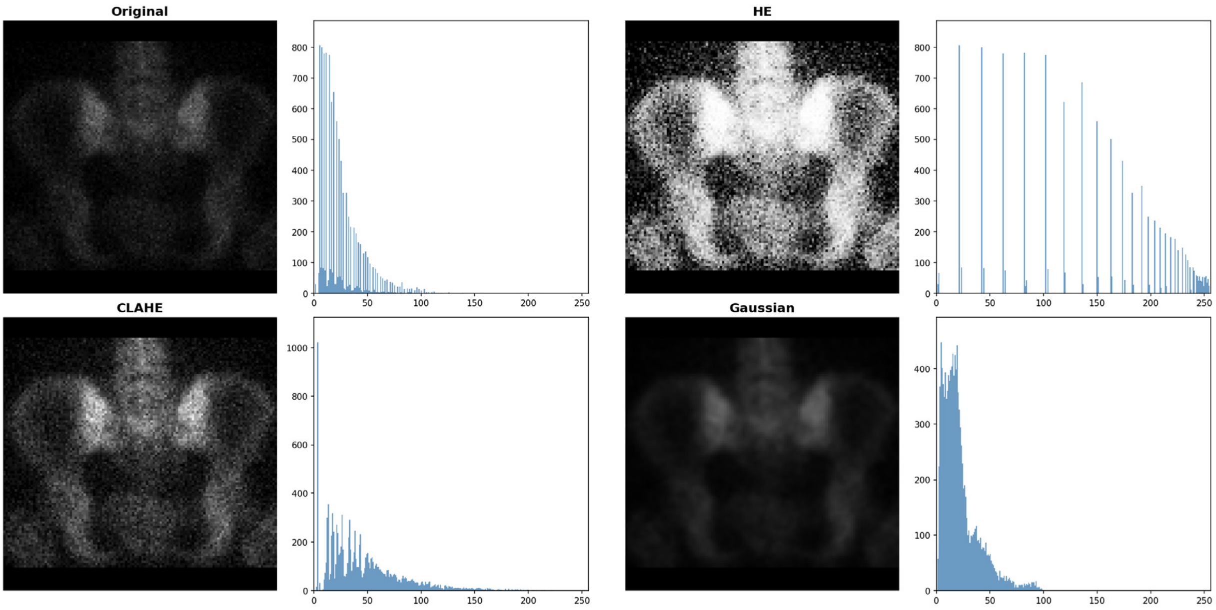

Fig. 1. Representative WBBS images after different preprocessing methods.

Results: Gaussian Blur achieved the highest mean AUC (0.9001 ± 0.0126), followed by Original (0.8954 ± 0.0106), CLAHE (0.8909 ± 0.0079), and HE (0.8780 ± 0.0109). HE showed significantly lower AUC than Original, CLAHE, and Gaussian Blur after Holm–Bonferroni correction ($p < 0.05$). However, no statistically significant differences were observed among Original, CLAHE, and Gaussian Blur. HE also demonstrated the lowest sensitivity (0.7195 ± 0.0774), whereas Original images showed the highest sensitivity (0.7968 ± 0.0294).

Conclusion: Global histogram equalization significantly degraded deep learning classification performance in WBBS images, whereas CLAHE and Gaussian Blur did not provide statistically significant improvements over Original images. These findings suggest that image preprocessing does not necessarily improve WBBS-based deep learning classification performance and that HE should be applied cautiously in bone metastasis classification tasks.

2026 KMS Summer Conference

심포지엄 고효율 전력변환용 Ni-Free 자성페이스트 소재 및 부품화 기술개발

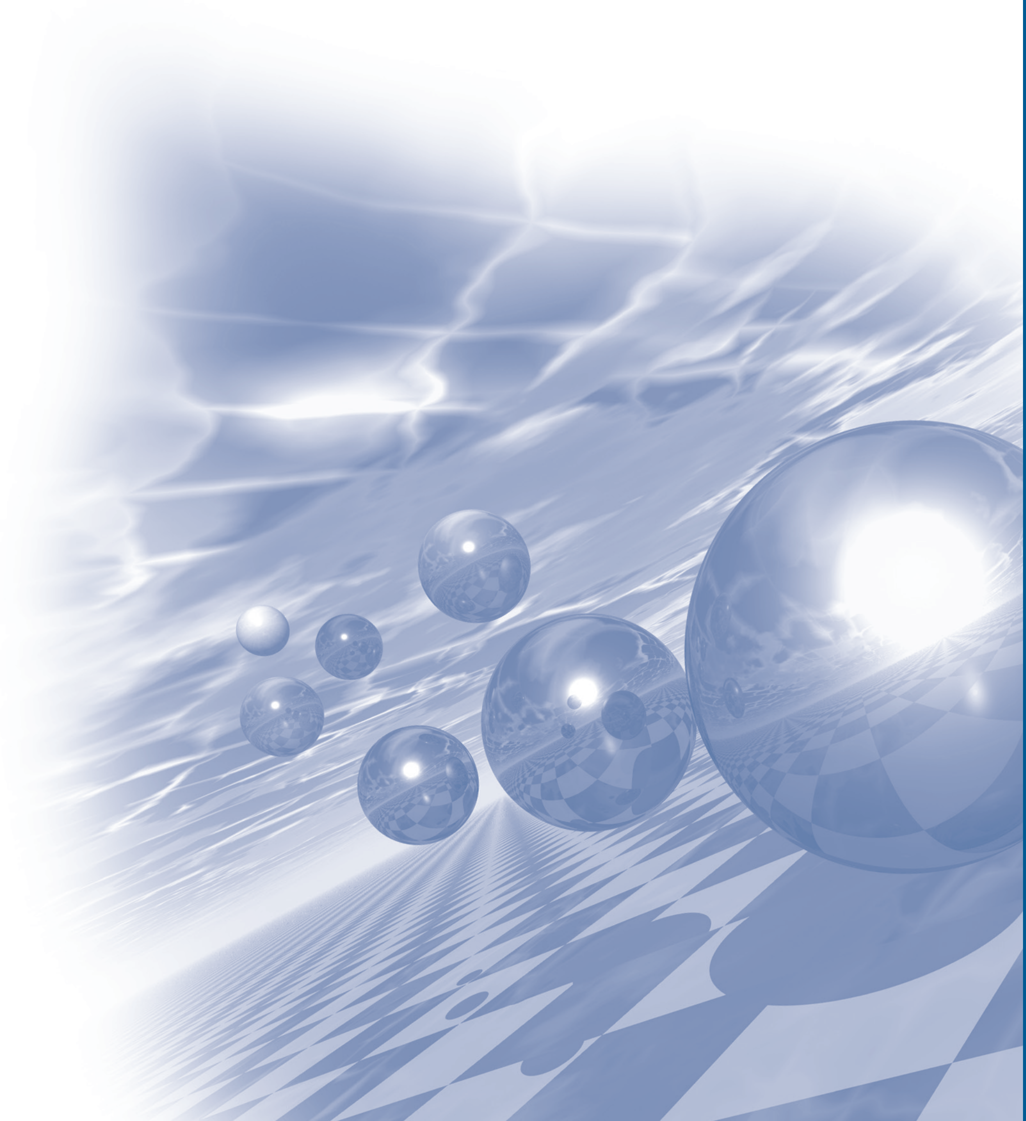

초S-2-1

고밀도/저손실 자성 페이스트 조성 설계기술 및 고효율 올인원 인덕터 제조기술 개발

김성배[*†]**, 이태경, 이정규, 박정현**
㈜창성 중앙연구소 신기술개발팀

전력변환장치의 고효율, 소형화 트렌드에 따라 핵심부품 인덕터의 요구 성능이 상승하고 있으며 이에 따라 높은 포화자화와 낮은 코어 손실을 동시에 만족하는 연자성 복합체의 중요성도 증대되고 있다. 최근에는 대표 연자성복합체 Fe-Ni(Permalloy)를 대체하는 Ni 저감 또는 Ni-free 기반 소재로의 개발이 활발히 진행되고 있다.

자성페이스트는 Ni-free 기반의 연자성재료로 올인원 인덕터의 연자성복합체(자성코어)로 활용 된다. 올인원 인덕터는 일정한 틀에 연자성재료와 권선체를 결합하여 일체형으로 제조하는 부품으로 공정 특성상 가압 공정이 배제된다. 따라서 기술 특성상 연자성복합체의 고밀도화를 달성하기 위한 자성페이스트 자체의 조성 설계 기술이 기반되어야 한다.

본 연구는 고밀도/저손실의 자성페이스트 조성 설계 기술 및 고효율 인덕터를 개발하는데 있으며 분말의 Multimodal 최적 배합으로 공극 최소화, 분말과 수지의 상용성 확보, 비정질 및 나노결정질 합금을 활용하여 고밀도화를 도모한다. 또한 분말의 산화층 제어, 비저항 세라믹 조성 최적화를 통한 분말 절연 코팅으로 철손을 저감하여 저손실 특성 확보를 도모한다.

이러한 기술 개발들은 자성페이스트의 분말 충진률 상승, 투자율 및 포화자화 상승, 철손 개선의 효과를 줄 수 있으며 인덕터의 고효율에 직결 될 수 있다. 또한 올인원 인덕터의 방열 구조 및 재료 활용을 통해서도 인덕터의 고효율화에 중점을 두고 있다.

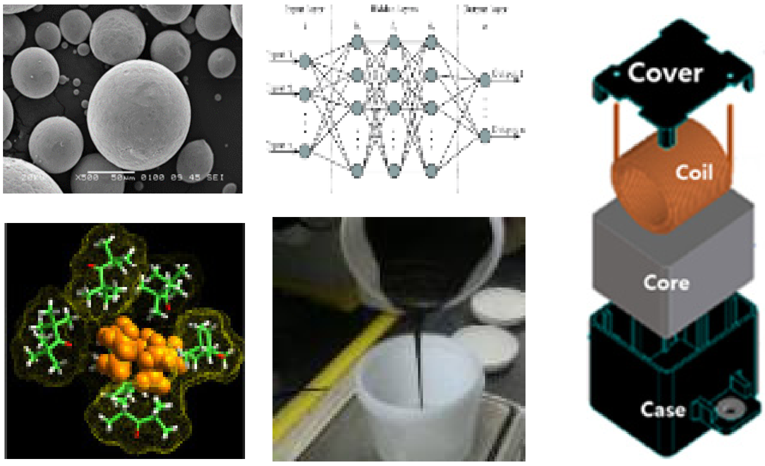

그림 1. 자성페이스트 / 올인원 인덕터

초S-2-2

수소연료전기 자동차 및 UAM용 200kW FDC 개발

Jaeho Na*†, Minjae Kim

Nextgrid, Korea

연료전기자동차 및 UAM 분야에서는 운항 거리 및 출력 향상을 위해 연료전지 시스템의 대용량화가 급격히 진행되고 있다. 이에 따라 연료전지 출력을 제어하는 FDC(Fuel Cell DC-DC Converter) 역시 200kW 급 이상의 고출력화가 요구되는 추세이다. 본 논문에서는 대용량화로 인해 필연적으로 증가하는 시스템의 부피와 무게 문제를 해결하기 위해, 고전력밀도 구현에 초점을 맞춘 컨버터 설계 및 자성체(인덕터) 경량화 설계 방안을 제안한다. 출력 용량이 2배로 증가함에 따라 발생하는 열 손실과 자성체 포화 문제를 해결하기 위한 최적의 설계 파라미터를 도출하였으며, 시뮬레이션을 통해 200kW 급 시스템에서의 고효율 및 경량화 성능을 검증하였다.

초S-2-3

패키징 인덕터를 적용한 5kW급 에너지저장장치 개발

김기현[1*†], 권효상[2]

[1]한솔테크닉스
[2]한솔에너지온

고효율 및 고전력 밀도의 에너지 저장장치(ESS)에 대한 수요가 지속적으로 증가함에 따라, 수동소자의 소형화 설계와 열 관리 기술의 중요성이 더욱 커지고 있다. 특히 인덕터는 전력변환 시스템에서 상당한 부피를 차지하며, 시스템 전체 효율, 전자파 간섭(EMI), 그리고 열 특성에 큰 영향을 미친다.

본 발표에서는 전력 밀도 향상, 열 안정성 확보 및 제조 효율 개선을 위해 패키징 인덕터를 적용한 5kW급 ESS 전력변환 시스템의 개발 내용을 설명한다.

현재 국책과제로 개발 중인 PCS(Power Conditioning System)는 양방향 DC-DC 컨버터와 PV 부스트 컨버터 회로에 패키징 인덕터를 적용하였다. 기존의 개별 자기소자 구조와 비교하여, 패키징 인덕터는 최적화된 내부 도체 레이아웃과 집적 패키징 기술을 통해 실장 효율을 향상시키고 권선 길이 단축 및 ESR이 감소하도록 설계되었으며, 열전달 구조와 방열 성능이 향상되도록 개발 하였다.

5kW급 ESS 시스템은 고주파 스위칭 기반으로 설계되었으며, 충전 및 방전 조건에서 성능 평가를 수행하였다. 실험 결과, 개발중인 패키징 인덕터는 기존 인덕터 대비 안정적인 전류 리플 특성을 유지하면서도 온도 상승을 감소시키고 체적 효율을 향상시키는 것으로 확인되었다. 또한 제안된 구조는 시스템의 소형화와 조립 생산성 향상에도 기여할 것으로 예상된다.

본 연구 결과를 통해 패키징 인덕터 기술이 고효율 및 고전력 밀도를 요구하는 차세대 소형 ESS 플랫폼에 효과적으로 적용될 수 있음을 확인하였으며, 향후에는 고효율 자기재료 적용, 방열 구조 개선 및 EMI 성능 확인 중심으로 추가 연구를 수행할 예정이다.

초S-2-3

페이스트 적용 인덕터의 손실 분석 및 열해석

Ju hee Cho*†, Hyo Joo Lim, Soo Yong Kim, Duck Shick Shin, Sang Taek Lee
Korea Electronics Technology Institute, Korea

전력변환기의 스위칭 주파수 증가를 통한 전력밀도 및 효율 향상을 위하여 적용되는 인덕터 또한 소형화에 대한 요구가 크게 증가하고 있는 추세이다. 이에 따라 인덕터는 고주파 환경에서 동작하여야 하고 고주파 환경에서 인덕터의 열적 거동을 예측하는 것은 매우 중요한 과제이다. 본 논문은 페이스트 소재를 적용한 인덕터의 열적 거동을 분석하기 위하여 인덕터의 고주파 특성을 고려한 손실 분석과 열 해석을 수행하였다. 고주파를 고려한 인덕터 손실 해석 방법을 제안하였으며 3가지 인덕터 모델의 손실 분석과 열해석을 통하여 각 모델의 장단점을 분석하였다.

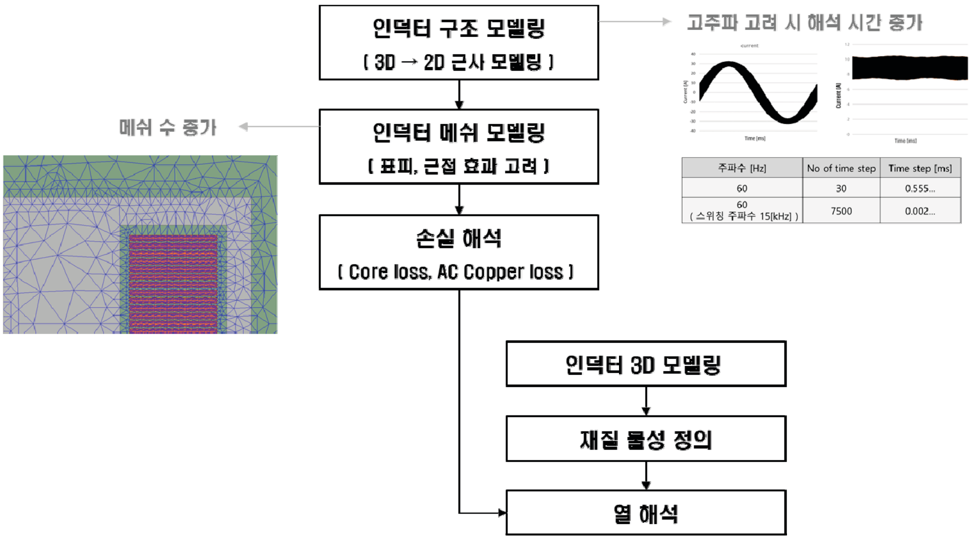

주파수 [Hz]	No of time step	Time step [ms]
60	30	0.555...
60 (스위칭 주파수 15[kHz])	7500	0.002...

Fig. 1. Current waveform

Acknowlegements

이 연구는 2023년도 산업통상자원부 및 산업기술 평가관리원(KEIT) 연구비 지원에 의한 연구임. (20026705)

References

[1] Jae-Wook Kim, “Study on Frequency Characteristics for Double-Layer Symmetric Spiral Inductor”, Journal of Korea Institute of Information, Electronics, and Communication Technology, vol. 15, no. 5, pp. 315-320,2022.

[2] Rachel S. Yang, Alex J. Hanson, Bradley A. Reese, Charles R. Sullivan, and David J. Perreault, “A Low-Loss Inductor Structure and Design Guidelines for High-Frequency Applications”, IEEE Trans. Power Electron, vol. 34, no. 10, pp.9993-10005, Oct. 2019.

[3] James Scoltock, Yiren Wang, Gerardo Calderon-Lopez, and Andrew J. Forsyth, “Rapid Thermal Analysis of Nanocrystalline Inductors for Converter Optimization”, IEEE Journal of Emerging and Selected Topics in Power Electronics, vol. 8, no. 3, Sep. 2020.

Author Index

Digests of the KMS 2026 Summer Conference
The Korean Magnetics Society
사단법인 한국자기학회

2026년 하계학술대회 논문개요집 제 36권 1호

(06130) 서울특별시 강남구 테헤란로 7길 22(역삼동635-4) 한국과학기술회관 신관 905호

TEL. (02)3452-7363, **FAX.** (02)3452-7364
E-mail. office@magnetics.or.kr, **Home-page.** www.magnetics.or.kr